Astronomy & Astrophysics manuscript no. Khouri˙et˙al˙Final
September 2, 2014
© ESO 2014

arXiv:1409.0396v1 [astro-ph.SR] 1 Sep 2014

The wind of W Hya as seen by Herschel.

II. The molecular envelope of W Hya

T. Khouri[1⋆], A. de Koter[1,2], L. Decin[1,2], L. B. F. M. Waters[1,3], M. Maercker[4,5], R. Lombaert[2], J. Alcolea[6], J. A. D. L. Blommaert[2,7], V. Bujarrabal[8], M. A. T. Groenewegen[9], K. Justtanont[4], F. Kerschbaum[10], M. Matsuura[11], K. M. Menten[12], H. Olofsson[4], P. Planesas[6], P. Royer[2], M. R. Schmidt[13], R. Szczerba[13], D. Teyssier[14], J. Yates[11]

[1] Astronomical Institute Anton Pannekoek, University of Amsterdam, PO Box 94249, 1090 GE Amsterdam, The Netherlands
[2] Instituut voor Sterrenkunde, KU Leuven, Celestijnenlaan 200D B-2401, 3001 Leuven, Belgium
[3] SRON Netherlands Institute for Space Research, Sorbonnelaan 2, 3584 CA Utrecht, The Netherlands
[4] Department of Earth and Space Sciences, Chalmers University of Technology, Onsala Space Observatory, SE-439 92 Onsala, Sweden
[5] Argelander Institute für Astronomie, Universität Bonn, Auf dem Hügel 71, 53121 Bonn, Germany
[6] Observatorio Astronómico Nacional (IGN), Alfonso XII N°3, E-28014 Madrid, Spain
[7] Department of Physics and Astrophysics, Vrije Universiteit Brussel, Pleinlaan 2, 1050 Brussels, Belgium
[8] Observatorio Astronómico Nacional (OAN-IGN), Apartado 112, E-28803 Alcalá de Henares, Spain
[9] Koninklijke Sterrenwacht van België, Ringlaan 3, B–1180 Brussel, Belgium
[10] University of Vienna, Department of Astrophysics, Türkenschanzstraße 17, 1180 Wien, Austria
[11] Dept. of Physics & Astronomy, University College London, Gower St, London WC1E 6BT, UK
[12] Max-Planck-Institut für Radioastronomie, Auf dem Hügel 69, 53121 Bonn, Germany
[13] N. Copernicus Astronomical Center, Rabiańska 8, 87-100 Toruń, Poland
[14] European Space Astronomy Centre, Urb. Villafranca del Castillo, PO Box 50727, E-28080 Madrid, Spain

Preprint online version: September 2, 2014

ABSTRACT

Context. The evolution of low- and intermediate-mass stars on the asymptotic giant branch (AGB) is mainly controlled by the rate at which these stars lose mass in a stellar wind. Understanding the driving mechanism and strength of the stellar winds of AGB stars and the processes enriching their surfaces with products of nucleosynthesis are paramount to constraining AGB evolution and predicting the chemical evolution of galaxies.
Aims. In a previous paper we have constrained the structure of the outflowing envelope of W Hya using spectral lines of the ^{12}CO molecule. Here we broaden this study by including an extensive set of H_2O and ^{28}SiO lines. It is the first time such a comprehensive study is performed for this source. The oxygen isotopic ratios and the ^{28}SiO abundance profile can be connected to the initial stellar mass and to crucial aspects of dust formation at the base of the stellar wind, respectively.
Methods. We model the molecular emission observed by the three instruments on board Herschel Space Observatory using a state-of-the-art molecular excitation and radiative transfer code. We also account for the dust radiation field in our calculations.
Results. We find an H_2O ortho-to-para ratio of $2.5\,^{+2.5}_{-1.0}$, consistent with what is expected for an AGB wind. The O^{16}/O^{17} ratio indicates that W Hya has an initial mass of about 1.5 $M_\odot$. Although the ortho- and para-H_2O lines observed by HIFI appear to trace gas of slightly different physical properties, we find that a turbulence velocity of 0.7 ± 0.1 km s^{-1} fits the HIFI lines of both spin isomers and those of ^{28}SiO well.
Conclusions. The modelling of H_2O and ^{28}SiO confirms the properties of the envelope model of W Hya, as derived from ^{12}CO lines, and allows us to constrain the turbulence velocity. The ortho- and para-$H_2^{16}O$ and ^{28}SiO abundances relative to H_2 are $(6^{+3}_{-2}) \times 10^{-4}$, $(3^{+2}_{-1}) \times 10^{-4}$, and $(3.3 \pm 0.8) \times 10^{-5}$, respectively, in agreement with expectations for oxygen-rich AGB outflows. Assuming a solar silicon-to-carbon ratio, the ^{28}SiO line emission model is consistent with about one-third of the silicon atoms being locked up in dust particles.

Key words. stars: AGB and post-AGB – circumstellar matter – stars: individual: W Hydrae – stars: mass-loss – line: formation – Stars: fundamental parameters

1. Introduction

Stars of low- and intermediate-mass ($\sim$0.8 to 8 $M_\odot$) populate the asymptotic giant branch (AGB) at the end of their lives. These luminous, extended, and cool objects develop a strong mass loss that controls their evolution from its onset. The driving of the wind is thought to be the result of a combination of pulsations and radiation pressure on dust grains (see e.g. Habing & Olofsson 2003). For carbon-rich AGB stars, this scenario is able to reproduce the observed mass-loss rates as the dust species that form in these environments are opaque enough and can exist close enough to the star to acquire momentum by absorbing infrared photons (Winters et al. 2000). However, for oxygen-rich AGB stars the situation seems more complex. The dust species found in these stars through infrared spectroscopy that would be able to drive the wind by absorption of stellar

⋆ *Send offprint requests to T. Khouri*
e-mail: theokhouri@gmail.com

photons cannot exist close enough to the star to be important for initiating the wind (Woitke 2006). A possible alternative is that the wind is driven through scattering of photons on large ($\sim 0.3\,\mu$m) translucent dust grains (Höfner 2008). Although this alternative scenario seems plausible and many dust species have been identified in oxygen-rich objects, it is still unclear which of these are actually responsible for driving the outflow (e.g. Bladh & Höfner 2012).

Characterizing both the physical structure and molecular and solid state composition of the outflow are crucial to understanding the physics underlying the wind driving. An important step forward in this understanding is the combined analysis of space and ground-based observations of multiple molecular species, covering a range of rotational excitation states of the ground vibrational level as wide as possible. Such data allow the determination of the flow properties from the onset of the wind close to the photosphere, to the outer regions, where molecules are eventually photodissociated by the interstellar radiation field. We have embarked on such an analysis for W Hya, a close-by oxygen-rich AGB star, observed in detail using the Herschel Space Observatory (hereafter *Herschel*; Pilbratt et al. 2010). In addition to the ^{12}CO lines, the observations reveal a rich $H_2^{16}O$ spectrum with over 150 observed lines, and a broad ^{28}SiO ladder, ranging from 137 to more than 2000 K in upper level excitation energy.

In Khouri et al. (2014, henceforth Paper I), we focussed on the analysis of the ^{12}CO ladder of rotational levels up to $J_{\rm up} = 30$. We used these carbon monoxide lines to determine the temperature and velocity structure of the wind, as well as the mass-loss rate. In the study presented here we focus on an analysis of lines from H_2O, including its isotopologues, and ^{28}SiO. The modelling of the H_2O isotopologues allows us to constrain the $^{17}O/^{16}O$ and $^{18}O/^{16}O$ ratios. The analysis of silicon in both the gas phase and solid phase allows us to assess the overall budget of this element and the condensation fraction of this species. This is a crucial issue for understanding the role of silicates for the wind driving mechanism. We also account for the contribution of the dust thermal emission to the radiation field when modelling the molecular emission. The main components of these grains are aluminum-oxides and silicates (e.g. Sharp & Huebner 1990).

Determining the ortho- and para-H_2O abundances is important for understanding the chemistry in the outermost layers of the star and the innermost regions of the envelope, where shocks can be important (Cherchneff 2006). For an AGB star with carbon-to-oxygen ratio of 0.75, Cherchneff (2006) finds the abundance ratio between ^{12}CO and $H_2^{16}O$ to be $\sim$ 12 and $\sim$ 1.6 for thermal equilibrium and non-equilibrium chemistry respectively. The H_2O ortho-to-para ratio is expected to be 3:1, reflecting the ratio of the statistical weights between the species, if the molecules are formed in a high-temperature ($T \gg 30$ K) and under local-thermodynamical equilibrium (Decin et al. 2010b). Studies of the $H_2^{16}O$ emission from W Hya have found a low ortho-to-para ratio of around 1 (e.g. Barlow et al. 1996; Justtanont et al. 2005; Zubko & Elitzur 2000). The uncertainties on these obtained ortho-to-para ratios are, however, at least of a factor of two.

The isotopic composition of the outflowing material contains much-needed information on the dredge-up processes that are an important part of giant branch and AGB evolution (e.g. Landre et al. 1990; El Eid 1994; Stoesz & Herwig 2003; Charbonnel & Lagarde 2010; Palmerini et al. 2011). Dredge-ups enrich the surface with isotopic species when convective streams in the star reach down to regions where the composition has been modified because of thermonuclear burning (see e.g. Iben & Renzini 1983; Iben 1975). The characteristics of the isotopic enrichment are expected to vary significantly over the evolution of low- and intermediate-mass stars and are found to be especially sensitive to stellar mass (Boothroyd et al. 1994) – the most important stellar property, which for AGB stars is notoriously difficult to constrain. Unfortunately, the dredge-up process in AGB stars cannot yet be modelled from first principles (Habing & Olofsson 2003), mainly because of the complex (and poorly understood) physics of convective and non-convective mixing (see e.g. Busso et al. 1999; Karakas 2010).

In Section 2 we provide general information on W Hya, the ^{12}CO model of Paper I, and the dataset that is used to constrain the $H_2^{16}O$ and ^{28}SiO properties. In Section 3, we discuss observed line shapes and provide details on the treatment of $H_2^{16}O$ and ^{28}SiO in our models, and how this treatment relates to that of ^{12}CO. Section 4 is devoted to presenting our model for $H_2^{16}O$ and for the lower abundance isotopologues. The model for ^{28}SiO is covered in Section 5. We discuss the results in Section 6 and we end with a summary.

2. Basis information, dataset, and model assumptions

2.1. W Hya

An overview of the literature discussing the stellar properties of W Hya, and the uncertainties in these properties, is presented in Paper I. We refer to this paper for details. We adopt a distance to the star of 78 pc (Knapp et al. 2003), implying a luminosity of 5400 $L_\odot$. Assuming that W Hya radiates as a black-body, our ^{12}CO analysis is consistent with an effective temperature of 2500 K, which leads to a stellar radius, $R_\star$, of 2.93×10^{15} cm or 1.96 AU. Whenever we provide the radial distance in the wind of W Hya in units of $R_\star$, this is the value we refer to. The ^{12}CO analysis presented in Paper I leads to a mass-loss rate of $1.3\times10^{-7}\ M_\odot\ {\rm yr}^{-1}$, consistent with the findings of Justtanont et al. (2005). Interestingly, on a scale that is larger than the ^{12}CO envelope, images of cold dust emission suggest W Hya had a substantially larger mass loss some 10^3–10^5 years ago (Cox et al. 2012; Hawkins 1990). In this work, we focus on the present-day mass-loss rate by modelling the gas-phase ^{28}SiO and H_2O emission, which probe the last 200 years at most. Variations in the mass-loss rate seen on larger timescales will be addressed in a future study.

W Hya features prominent rotational $H_2^{16}O$ emission, first reported by Neufeld et al. (1996) and Barlow et al. (1996), using data obtained with the *Infrared Space Observatory* (ISO; Kessler et al. 1996). Additional data were obtained by Justtanont et al. (2005), using *Odin* (Nordh et al. 2003), and by Harwit & Bergin (2002), using SWAS (Melnick et al. 2000). The analysis by the authors mentioned above and by others (Zubko & Elitzur 2000; Maercker et al. 2008, 2009) point to a quite high $H_2^{16}O$ abundance relative to H_2, ranging from 10^{-4} to a few times 10^{-3}. The ortho-to-para H_2O ratio reported by most studies is usually in-between 1 and 1.5, which is significantly lower than the expected value of three, for H_2O formed at high temperatures ($T \gg 30$ K) and in local-thermodynamical equilibrium.

^{28}SiO lines of the vibrational excited $v = 1$ and $v = 2$ state show maser emission and have been intensively studied (see e.g. Imai et al. 2010; Vlemmings et al. 2011). Ground vibrational lines do not suffer from strong amplification

and are better probes of the silicon abundance. Studies of this molecule (e.g. González Delgado et al. 2003; Bieging et al. 2000; Bujarrabal et al. 1986) suggest ^{28}SiO is depleted from the gas, probably due to the formation of silicate grains. Spatially resolved data of the $v = 0, J = 2 - 1$ line have been presented by Lucas et al. (1992). The authors determined the half-intensity radius of this transition to be 0.9 arcseconds. From model calculations, González Delgado et al. (2003) conclude that the half-intensity radius determined by Lucas et al. (1992) is approximately three times smaller than the radius where the ^{28}SiO abundance has decreased to 37% of its initial value.

The dust envelope of W Hya has been imaged by Norris et al. (2012) using aperture-masking polarimetric interferometry. They discovered a close-in shell of large ($\sim 0.3\,\mu$m) and translucent grains which might be responsible for driving the outflow through scattering (Höfner 2008). Unfortunately, the composition of the observed grains could, not be unambiguously identified. W Hya has also been observed in the near-infrared using MIDI/VLTI (Zhao-Geisler et al. 2011). This revealed that the silicate dust emission must come from an envelope with an inner radius of 50 AU (or 28 $R_\star$). Zhao-Geisler et al. (2011) also argue that Al_2O_3 grains and H_2O molecules close to the star are responsible for the observed increase in diameter at wavelengths longer than 10 μm.

2.2. Dataset

W Hya was observed by all three instruments onboard *Herschel* in the context of the guaranteed-time key programs HIFISTARS (Menten et al. 2010) and MESS (Groenewegen et al. 2011). These are the Heterodyne Instrument for the Far Infrared (HIFI; de Graauw et al. 2010), the Spectral and Photometric Imaging Receiver Fourier-Transform Spectrometer (SPIRE; Griffin et al. 2010), and the Photodetector Array Camera and Spectrometer (PACS; Poglitsch et al. 2010). The data reduction procedure of the PACS and SPIRE data is outlined in Paper I ; that of HIFI is presented by Justtanont et al. (2012).

We applied two methods to identify the $H_2^{16}O$ and ^{28}SiO lines. The ^{28}SiO lines were identified in very much the same way as the ^{12}CO lines presented in Paper I: we inspected the spectra at the wavelengths of the ^{28}SiO transitions, identified the lines and measured their fluxes. $H_2^{16}O$, however, has a plethora of transitions that, moreover, are not regularly spaced in frequency, as are the ones of ^{12}CO and ^{28}SiO. Our approach in this case was to calculate spectra with different values for the $H_2^{16}O$-envelope parameters and compare these to the observations. Transitions that were predicted to stand out from the noise were identified and extracted.

In order to extract the integrated fluxes from the PACS spectrum, we fitted Gaussians to the identified transitions using version 11.0.1 of *Herschel* interactive processing environment (HIPE[1]). For extracting transitions measured by SPIRE, we used the script *Spectrometer Line Fitting* available in HIPE. The script simultaneously fits a power law to the continuum and a cardinal sine function to the lines in the unapodized SPIRE spectrum. The spectral resolution of both instruments is smaller than twice the terminal velocity of W Hya ($\upsilon_\infty = 7.5$ kms^{-1}; see Table 1). Therefore, what may appear to be a single observed line might be a blend of two or more transitions. We removed such blended lines from our analysis by flagging them as blends whenever two or more transitions were predicted to be formed closer together than the native full width at half-maximum (FWHM) of the instrument, or when the FWHM of the fitted Gaussian was 20% or more larger than the expected FWHM for single lines. For PACS, a total of 50 ortho-$H_2^{16}O$, 24 para-$H_2^{16}O$, and only 1 ^{28}SiO unblended transitions were extracted. The ^{28}SiO transitions that lie in the spectral region observed by PACS are high excitation lines ($J_{\rm up} > 35$). These are weak compared to the much stronger $H_2^{16}O$ lines and are below the detection limit of the PACS spectrum for $J_{\rm up} > 38$. For SPIRE, 15 ortho-$H_2^{16}O$, 20 para-$H_2^{16}O$ and 24 ^{28}SiO lines were extracted and not flagged as blends. Properties of all $H_2^{16}O$ transitions measured by PACS and those of ^{28}SiO measured by all instruments are given in Appendix B.

The transitions observed with HIFI are spectrally resolved. This gives valuable information on the velocity structure of the flow. Because of the high spectral resolution the lines are easily identified and their total fluxes can be measured accurately. In Table 2, we list the integrated main beam brightness temperatures and the excitation energy of the upper level for the observed transitions. HIFI detected ten ortho-$H_2^{16}O$ transitions, two of which are clearly masering, six para-$H_2^{16}O$ transitions, one of which is clearly masering, five ^{28}SiO transitions, three of which are from vibrationally excited states and appear to be masering, two transitions of ortho-$H_2^{17}O$ and ^{29}SiO, and one transition each of ortho-$H_2^{18}O$, para-$H_2^{17}O$, para-$H_2^{18}O$ and ^{30}SiO. We have not included the rarer isotopologues of SiO, ^{29}SiO and ^{30}SiO, in our model calculations. The vibrationally excited lines from ^{28}SiO probe high temperature gas ($T \sim 2000$ K) which is very close to the star and were not included in our analysis. The upper level excitation energies of the ^{28}SiO ground-vibrational lines range from 137 to 1462 K and these transitions probe the gas temperatures in which silicates are expected to condense, $T \sim 1000$ K (e.g. Gail & Sedlmayr 1999).

2.2.1. $H_2^{16}O$ masers

The already challenging task of modelling $H_2^{16}O$ emission is further complicated by the fact that this molecule has the predisposition to produce maser emission. Matsuura et al. (2013) found that for the oxygen-rich supergiant VY CMa 70% of the $H_2^{16}O$ lines in the PACS and SPIRE spectra are affected by population inversions. In our line emission code we artificially suppress strong stimulated emission and we have therefore excluded from the present analysis lines that show masering in at least one of our models. In the PACS data, four transitions were excluded. Those are the ones at 133.549, 159.051 and 174.626 μm of ortho-$H_2^{16}O$ and 138.528 μm of para-$H_2^{16}O$. The intensity of the ortho-$H_2^{16}O$ transition at 73.415 was under-predicted by more than a factor of three by all models. Although this line is not masering in any of our models, the discrepancies are so large that we suspect missing physics to be responsible. We have also excluded this line from the analysis. In four of the remaining PACS lines, we do find modest population inversions for some of the models. These, however, do not appear to have a strong impact on the strength of the lines and the transitions were not excluded. For the SPIRE lines, the case is worse. About 70 % of the lines – in agreement with the results reported for VY CMA by Matsuura et al. (2013) – present population inversions. The intensity of most of these lines was strongly under-predicted by our models. This is a much higher fraction than the less than 10% seen for PACS. To be on the safe side, we decided not to include SPIRE data at all in our calculations for $H_2^{16}O$. As a result of this mismatch a comprehensive identification of the $H_2^{16}O$ lines

[1] HIPE is available for download at http://herschel.esac.esa.int/hipe/

in the SPIRE spectrum was not possible and we do not present extracted line fluxes for $H_2^{16}O$ lines obtained by this instrument.

2.2.2. Comparison between the total line fluxes measured by HIFI, SPIRE and PACS

Some of the lines were observed by more than one instrument, either by HIFI and SPIRE or by HIFI and PACS. In Table 3 we present a comparison of the observed total line fluxes. The antennae temperatures observed by HIFI were converted to flux units assuming that the emission is not spatially resolved by the telescope. We find that the fluxes of $H_2^{16}O$ lines as detected by HIFI are systematically lower than those by both SPIRE and PACS.

SPIRE lines are typically 25% stronger than those of HIFI. This difference may be due to uncertainties in the flux calibration of both instruments and in the baseline fitting of the spectra. Small blends and pointing errors can also account for some of the observed differences. A flux loss of less than 10% is expected from the pointing errors in the HIFI observations. The different shapes of the response function of the instruments may also have a significant effect.

The three lines measured jointly by PACS and HIFI are more than 2–3 times stronger in the PACS traces than in the HIFI spectra. The cross-calibration problem of PACS and HIFI is known, but is not yet resolved. It is often reported as a flux mismatch between the ^{12}CO lines observed by both instruments (Puga et al. in prep.). For W Hya we find that the mismatch between predicted and PACS line fluxes correlates with wavelength, becoming larger for longer wavelengths. At the long wavelength end of the PACS spectral range (which is where PACS and HIFI spectra overlap) the discrepancy strongly increases. Since the HIFI observations are much less susceptible to line blending and the HIFI line fluxes in this overlap region agree much better with the trends predicted by our models than the line fluxes measured by PACS, we decided to exclude these PACS lines from our analysis, and to use the HIFI lines instead.

2.3. Modelling strategy and ^{12}CO model

Here, we focus on modelling the emission of ortho-$H_2^{16}O$, para-$H_2^{16}O$, ortho-$H_2^{18}O$, para-$H_2^{18}O$, ortho-$H_2^{17}O$, para-$H_2^{17}O$ and ^{28}SiO. The molecular data used in our calculations are described in Appendix A. Our model is based on the envelope structure and dust model obtained in Paper I, which was obtained from the analysis of ^{12}CO lines, observed with *Herschel*, APEX, SMT and SEST, and of the dust emission. The ^{12}CO transitions modelled in Paper I probe a large range in excitation temperature and, therefore, the full extent of the outflowing ^{12}CO envelope, from the regions close to the star where the wind is accelerated, to the outer regions where ^{12}CO is photo-dissociated. The dust properties were constrained by modelling the thermal emission spectrum observed by ISO with the continuum radiative-transfer code MCMax (Min et al. 2009). The composition and radial distribution of the dust are used as inputs to the modelling of the molecular species, for which we employ GASTRoNOoM (Decin et al. 2006, 2010a). The coupling between dust and gas is treated as described by Lombaert et al. (2013). The main parameters of the ^{12}CO model are listed in Table 1.

In Paper I, we found that the ^{12}CO envelope has to be smaller than predicted for our model to better fit the high- ($J_{\rm up} \geq 6$) and low-excitation ($J_{\rm up} < 6$) ^{12}CO transitions simultaneously. The size of the ^{12}CO envelope is set in our model by the parameter $R_{1/2}$ (Mamon et al. 1988), which represents the radius at which the ^{12}CO abundance has decreased by half. We note that this discrepancy between model and observations in the outer wind is not expected to affect the modelled $H_2^{16}O$ or ^{28}SiO lines, since these molecules occupy a much smaller part of the envelope than ^{12}CO, see Fig. 1.

Table 1. Model parameters of W Hya as derived in Paper I.

Parameter	Best Fit
dM/dt [10^{-7} $M_\odot$ yr^{-1}]	1.3 ± 0.5
υ_∞ [km s^{-1}]	7.5 ± 0.5
ϵ	0.65 ± 0.05
$\upsilon_{\rm turb}$ [km s^{-1}]	1.4 ± 1.0
$f_{\rm CO}$	4×10^{-4}
$R_{1/2}$	0.4
T_* [K]	2500

Notes. ϵ is the exponent of the temperature power law and $R_{1/2}$ is the radius where the CO abundance has decreased by half.

Furthermore, to properly represent the PACS and HIFI transitions excited in the inner part of the wind, our best model requires a value of 5.0 for the exponent of the β-type velocity law (see Equation 1),

$$\upsilon(r) = \upsilon_\circ + (\upsilon_\infty - \upsilon_\circ)\left(1 - \frac{r_\circ}{r}\right)^\beta . \quad (1)$$

This corresponds to a slow acceleration of the flow in this part of the envelope. However, this high value of β underpredicts the width of the ^{12}CO $J = 6-5$ transition, while predicting well the width of lower excitation transitions ($J_{\rm up} < 6$). This indicates a more rapid acceleration between the formation region of transitions $J = 10-9$ and $J = 6-5$ than considered in our $\beta = 5.0$ model. This could be due to the addition of extra opacity in the wind at distances beyond where the $J = 10-9$ transition forms, which is roughly inside 50 $R_\star$. As the $H_2^{16}O$ and ^{28}SiO envelopes are smaller than the excitation region of the ^{12}CO $J_{\rm up} = 6$ level, emission from these two molecules comes from a wind region that is well described by a $\beta = 5.0$ velocity law (see also Fig. 1).

Our dust model is motivated by the work of Justtanont et al. (2004, 2005) and adopts a dust mass-loss rate of 2.8×10^{-10} $M_\odot$ yr^{-1}. Astronomical silicates, amorphous aluminum oxide (Al_2O_3), and magnesium-iron oxide (MgFeO) account for 58, 34, and 8% of the dust mass, respectively. The optical constants for astronomical silicates are from Justtanont & Tielens (1992), those for amorphous aluminum oxide and magnesium-iron oxide were retrieved from the University of Jena database and are from the works of Begemann et al. (1997) and Henning et al. (1995).

3. Comparisons between ^{12}CO, $H_2^{16}O$ and ^{28}SiO

3.1. Photodissociation radii

^{12}CO, ^{28}SiO, and $H_2^{16}O$ are formed in the atmosphere of the AGB star and the fate of these molecules is to become dissociated in the outer envelope by interstellar UV photons, causing their abundances to decrease sharply. The radius where dissociation sets in is different for each molecule and depends on molecular and circumstellar parameters and on the spectral shape of the interstellar radiation field.

Dust condensation might play a role in shaping the abundance profile of a molecule if the conditions for condensation are met before dissociation sets in. For W Hya we expect ^{28}SiO to condense and form silicate grains. ^{12}CO and $H_2^{16}O$ abundances

Table 3. Observed total line fluxes of $H_2^{16}O$ and ^{28}SiO transitions observed by two different *Herschel* instruments, HIFI and SPIRE or PACS. The final column lists the flux of either SPIRE or PACS, relative to HIFI.

Transition	ν_0 [GHz]	λ [μm]	E_{up} [K]	Flux HIFI [W m^{-2}]	Flux SPIRE [W m^{-2}]	Flux PACS [W m^{-2}]	F(Other)/F(HIFI)
ortho-$H_2^{16}O$							
$1_{1,0} - 1_{0,1}$	556.936	538.29	61	3.8×10^{-17}	5.5×10^{-17}	-	1.45
$5_{3,2} - 4_{4,1}$	620.701	482.99	732	6.5×10^{-17}	7.4×10^{-17}	-	1.14
v2=1,$1_{1,0} - 1_{0,1}$	658.007	455.61	2360	2.4×10^{-16}	3.0×10^{-16}	-	1.25
$3_{1,2} - 3_{0,3}$	1097.365	273.19	249	1.1×10^{-16}	1.3×10^{-16}	-	1.18
$3_{1,2} - 2_{2,1}$	1153.127	259.98	249	3.0×10^{-16}	3.7×10^{-16}	-	1.23
$3_{2,1} - 3_{1,2}$	1162.911	257.79	305	1.2×10^{-16}	1.8×10^{-16}	-	1.50
$3_{0,3} - 2_{1,2}$	1716.769	174.63	197	5.4×10^{-16}	-	1.3×10^{-15}	2.41
$5_{3,2} - 5_{2,3}$	1867.749	160.51	732	1.2×10^{-16}	-	2.8×10^{-16}	2.33
para-$H_2^{16}O$							
$2_{1,1} - 2_{0,2}$	752.033	398.64	137	6.6×10^{-17}	8.1×10^{-17}	-	1.23
$5_{2,4} - 4_{3,1}$	970.315	308.96	599	2.5×10^{-16}	3.6×10^{-16}	-	1.44
$2_{0,2} - 1_{1,1}$	987.927	303.46	101	2.3×10^{-16}	2.9×10^{-16}	-	1.26
$1_{1,1} - 0_{0,0}$	1113.343	269.27	53	2.2×10^{-16}	2.2×10^{-16}	-	1.00
$4_{2,2} - 4_{1,3}$	1207.639	248.25	454	4.9×10^{-17}	6.7×10^{-17}	-	1.21
$6_{3,3} - 6_{2,4}$	1762.043	170.14	952	5.3×10^{-17}	-	1.7×10^{-16}	3.21
^{28}SiO							
J=14-13	607.608	493.40	218.8	2.1×10^{-17}	2.0×10^{-17}	-	0.95
J=16-15	694.294	431.79	283.3	2.5×10^{-17}	2.4×10^{-17}	-	0.96

Table 2. H_2O and ^{28}SiO transitions observed by HIFI for W Hya.

Transitions	ν_0 [GHz]	E [K]	$\int T_{MB}\, dv$ [K km s^{-1}]
o-$H_2^{16}O_{v=0,5_{3,2}-5_{2,3}}$	1867.749	732.0	5.3 ±0.6
o-$H_2^{16}O_{v=0,7_{3,4}-7_{2,5}}$	1797.159	1212.0	2.3 ±0.3
o-$H_2^{16}O_{v_2=1,2_{1,2}-1_{0,1}}$	1753.914	2412.9	2.2 ±0.6
o-$H_2^{16}O_{v=0,3_{0,3}-2_{1,2}}$	1716.769	196.8	24.9±0.3
o-$H_2^{16}O_{v=0,3_{2,1}-3_{1,2}}$	1162.911	305.2	8.1 ±0.3
o-$H_2^{16}O_{v=0,3_{1,2}-2_{2,1}}$	1153.127	249.4	21.1±0.4
o-$H_2^{16}O_{v=0,3_{1,2}-3_{0,3}}$	1097.365	249.4	8.0 ±0.2
o-$H_2^{16}O_{v_2=1,1_{1,0}-1_{0,1}}$	658.007	2360.3	28.9±0.1
o-$H_2^{16}O_{v=0,5_{3,2}-4_{4,1}}$	620.701	732.1	8.4 ±0.1
o-$H_2^{16}O_{v=0,1_{1,0}-1_{0,1}}$	556.936	61.0	5.4 ±0.1
o-$H_2^{17}O_{v=0,3_{0,3}-2_{1,2}}$	1718.119	196.4	1.0 ±0.2
o-$H_2^{17}O_{v=0,3_{1,2}-3_{0,3}}$	1096.414	249.1	0.5 ±0.1
o-$H_2^{18}O_{v=0,3_{1,2}-3_{0,3}}$	1095.627	248.7	1.5 ±0.1
p-$H_2^{16}O_{v=0,6_{3,3}-6_{2,4}}$	1762.043	951.8	2.4 ±0.6
p-$H_2^{16}O_{v=0,4_{2,2}-4_{1,3}}$	1207.639	454.3	3.3 ±0.5
p-$H_2^{16}O_{v=0,1_{1,1}-0_{0,0}}$	1113.343	53.4	15.4±0.1
p-$H_2^{16}O_{v=0,2_{0,1}-1_{1,1}}$	987.927	100.8	18.6±0.2
p-$H_2^{16}O_{v=0,5_{2,4}-4_{3,1}}$	970.315	598.8	20.9±0.1
p-$H_2^{16}O_{v=0,2_{1,1}-2_{0,2}}$	752.033	136.9	7.0 ±0.1
p-$H_2^{17}O_{v=0,1_{1,1}-0_{0,0}}$	1107.167	53.1	0.5 ±0.1
p-$H_2^{18}O_{v=0,1_{1,1}-0_{0,0}}$	1101.698	52.9	1.5 ±0.1
$^{28}SiO_{v=1,J=23-22}$	990.355	2339.9	0.4 ±0.1
$^{28}SiO_{v=0,J=16-15}$	694.275	283.3	2.9 ±0.1
$^{28}SiO_{v=1,J=15-14}$	646.429	2017.4	0.2 ±0.04
$^{28}SiO_{v=0,J=14-13}$	607.599	218.8	2.8 ±0.1
$^{28}SiO_{v=1,J=13-12}$	560.326	1957.4	0.3 ±0.1

should not be affected by such depletion and we assume their abundances to be constant up to the point where dissociation starts. For ^{28}SiO we consider different abundance profiles, mimicking depletion due to silicate formation (see Sect. 5).

Dissociation radii are usually poorly constrained. In our ^{12}CO model presented in Paper I, we find that for W Hya the ^{12}CO envelope is likely smaller than expected for a standard interstellar radiation field. Our results point to an envelope with ^{12}CO being fully dissociated at roughly 800 $R_\star$. We have assumed dissociation profiles for $H_2^{16}O$ and ^{28}SiO of the type

$$f(r) = f^\circ\, e^{-(r/r_e)^p}, \qquad (2)$$

where the standard value of the exponent p is 2 and r_e is the e-folding radius, the radius at which the abundance has decreased by a factor e from its initial value. $H_2^{16}O$ is expected to dissociate closer to the star than ^{12}CO (e.g. Netzer & Knapp 1987). Groenewegen (1994) argues that $H_2^{16}O$ emission should come from within roughly 100 $R_\star$, from considering studies of OH density profiles in AGB stars. This limit corresponds to an abundance profile with e-folding radius of 65 $R_\star$, or 1.8×10^{15} cm. For ^{28}SiO, there are no theoretical estimates that give its dissociation radius in terms of envelope parameters. That said, González Delgado et al. (2003) modelled low-excitation ^{28}SiO transitions and determined the e-folding radius to be $r_e = 2.4 \times 10^{15}$ cm for W Hya, which corresponds to roughly 85 $R_\star$ in the context of our model. At about 200 $R_\star$ all of the ^{28}SiO will then have disappeared. We adopt these values. They show that the ^{28}SiO envelope is comparable in size to the H_2O envelope and that both are considerably smaller than the CO envelope. Because the ^{28}SiO transitions modelled by us are formed mostly deep inside the ^{28}SiO envelope, we expect the problem of constraining the ^{28}SiO dissociation radius to have little impact on our results.

In Fig. 1, we plot the normalized abundance profiles of ^{12}CO, ^{28}SiO and $H_2^{16}O$ compared to the excitation region of the ^{12}CO transitions observed by HIFI. This shows that the $H_2^{16}O$ and ^{28}SiO emissions probe a relatively small region of the envelope compared to ^{12}CO emission.

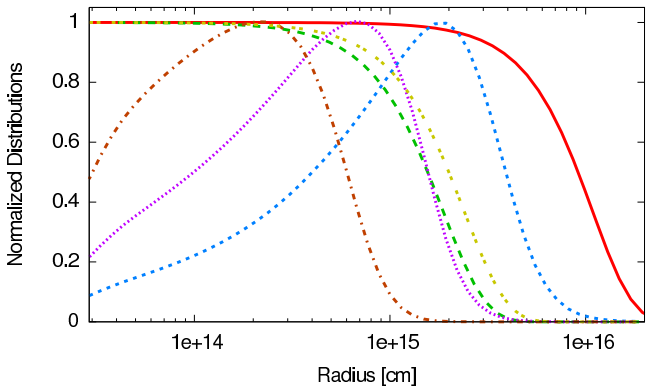

Fig. 1. The normalized abundance profile of $H_2^{16}O$ (long-dashed green), ^{28}SiO (double-short-dashed yellow) and ^{12}CO (solid red) are compared to the normalized populations of levels $J = 16$ (dashed-dotted brown), $J = 10$ (dotted purple) and $J = 6$ (short-dashed blue) of ^{12}CO.

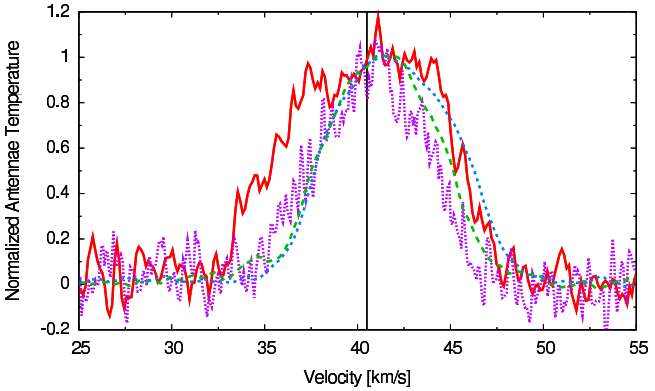

Fig. 2. Observed line shapes of the transitions $J = 16-15$ (dotted purple) and $J = 10-9$ (solid red) of ^{12}CO, $J = 14-13$ of ^{28}SiO (long-dashed green), and $1_{1,0}-0_{0,1}$ of ortho-$H_2^{16}O$ (short-dashed blue). The vertical line marks the adopted $\upsilon_{LSR} = 40.4\,km\,s^{-1}$.

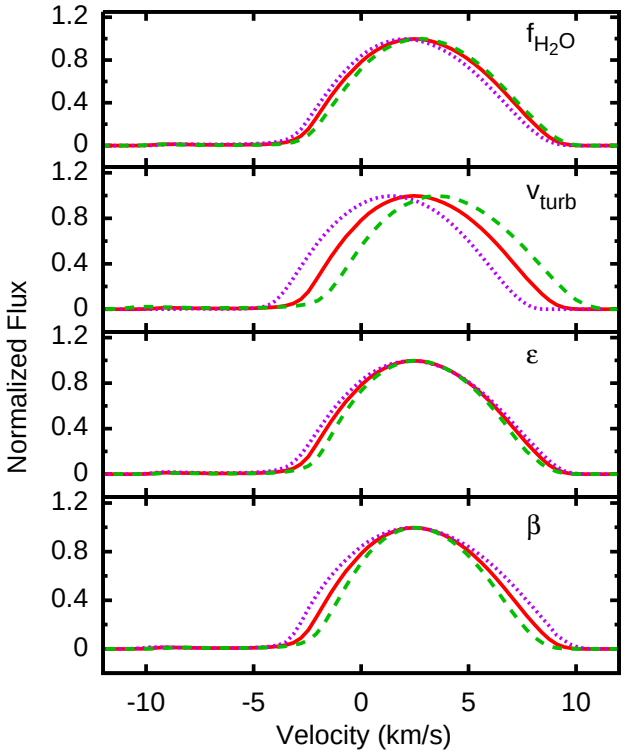

Fig. 3. The effects of varying the $H_2^{16}O$ abundance, the turbulence velocity, the temperature power law exponent and the velocity power law exponent on the normalized line strength are shown for o-$H_2^{16}O$ ($1_{1,0}-1_{0,1}$). The standard model is represented by the red line in each panel, it has its values given in Table 1 and $f_{H_2O} = 4 \times 10^{-4}$. The short-dashed purple and the long-dashed green represent models with respectively: $f_{H_2O} = 1 \times 10^{-4}$ and 1.6×10^{-3} in the first panel; $\upsilon_{turb} = 0.8$ and 2.0 km s^{-1} in the second panel; $\epsilon = 0.2$ and 1.1 in the third panel; and $\beta = 1.5$ and 10 in the fourth panel. All other parameters have the same value as the standard model. We note that varying υ_{turb} has the effect of a line shift.

3.2. Observed line shapes: blue wing absorption

Fig. 2 shows the spectrally resolved profiles of the lowest excitation transitions of $H_2^{16}O$ and ^{28}SiO, as observed by HIFI, and of the $J = 16-15$ and $10-9$ transitions of ^{12}CO. The adopted local-standard-of-rest velocity of 40.4 km s^{-1} was derived by Khouri et al. (2014) by modelling the ^{12}CO and ^{13}CO transitions. The plotted $H_2^{16}O$ and ^{28}SiO lines are expected to form in about the same region of the envelope as the pure rotational $J = 10-9$ line of ^{12}CO, as they are low-excitation transitions expected to be formed in the outer parts of the ^{28}SiO and $H_2^{16}O$ envelopes. The ^{12}CO $J = 10-9$ transition shows emission up to the same expansion velocity in the red- and blue-shifted wings. The $H_2^{16}O$ and ^{28}SiO transitions, however, show very asymmetrical line profiles with emission extending to larger velocities in the red-shifted wing than on the blue-shifted wing. To show the effect of differences in line forming region (which cannot be the cause of this behaviour, as the lines are selected to form in about the same part of the flow), we also show the ^{12}CO $J = 16-15$ line profile. This line forms more to the base of the outflow. The profile is narrower on both sides of line centre.

Huggins & Healy (1986) studied the line shapes of transitions $J = 2-1$ and $J = 1-0$ of ^{12}CO in IRC +10216 in comparison to the line shape of the optically thinner ^{13}CO $J = 2-1$ line. The authors observed asymmetries between the ^{12}CO and ^{13}CO lines and concluded that these were due to the higher optical depths in the ^{12}CO lines. They found the effect to be strongly dependent on the turbulence velocity in the line formation region. In Fig. 2, the differences between H_2O and ^{28}SiO on the one hand and ^{12}CO $J = 10-9$ on the other hand also arise as a result of differences in line optical depth, and the presence of a turbulence velocity field. The ^{12}CO radial optical depth at line centre is about unity for the transitions discussed. The Einstein coefficient for spontaneous emission of the $H_2^{16}O$ and ^{28}SiO transitions modelled here are typically at least an order of magnitude larger than that of ^{12}CO. The ^{28}SiO $J = 16-15$ and $14-13$ lines have even two orders of magnitude higher values. As a result, higher optical depths are built-up for ^{28}SiO and $H_2^{16}O$ transitions than for ^{12}CO transitions, even when the different abundances are taken into account. The effect is important even in the wind of a low mass-loss rate AGB star such as W Hya, and it reveals itself by the shift in the observed line centre velocity with respect to the υ_{LSR} of the source.

In Fig. 3, we show that υ_{turb} indeed affects strongly the observed behaviour of $H_2^{16}O$ and ^{28}SiO. The o-$H_2^{16}O$ ($1_{1,0} - 1_{0,1}$) transition is shown for models based on the best ^{12}CO model obtained in Paper I. We varied either the $H_2^{16}O$ abundance, the turbulence velocity in the envelope, υ_{turb}, the exponent of the tem-

Table 4. Turbulence velocities and abundances relative to H_2 considered in the models studying the effects of $H_2^{16}O$.

Parameter	Values
$\upsilon_{\rm turb}$ [km s^{-1}]	0.5, 0.8, 1.1, 1.4
f(o-$H_2^{16}O$)	(1, 2, 4, 5, 6, 7, 8, 10, 12, 16) $\times 10^{-4}$
f(p-$H_2^{16}O$)	(1, 2, 3, 4, 5, 6, 8) $\times 10^{-4}$

perature power law, ϵ, or the exponent of the velocity power law, β. Although all these parameters have an impact on the $H_2^{16}O$ line shapes or central peak position, it is the turbulence velocity that causes a systematic shift of the line centre position. We stress that varying these parameters does have a significant effect on the line strength. To bring out the effects on profile shape and profile shift, we have normalized the lines. As pointed out by Huggins & Healy (1986), the magnitude of the shift is mainly set by and can be used to determine the value of the turbulence velocity in the line formation region.

4. $H_2^{16}O$ model

We calculated models using the parameters found in Paper I for different values of the ortho- and para-$H_2^{16}O$ abundance and the turbulence velocity in the wind. The turbulence velocity was included as a free parameter since it was clear from the first calculated $H_2^{16}O$ profiles that the originally assumed value ($\upsilon_{\rm turb}$ = 1.4 km s^{-1}; see Table 1) was too large to match the line-centre shifts seen in the line profiles obtained with HIFI (see Sect. 3.2). The $H_2^{16}O$ abundance at a radius r is given by Equation 2. The value adopted by us for the H_2O dissociation radius is that given by Groenewegen (1994). Our model calculations, however, show that the derived $H_2^{16}O$ abundance is not strongly affected by the assumed dissociation radius.

The turbulence velocity and the abundance of each spin isomer constitute a degeneracy. We can, however, determine with a good accuracy the value of the turbulence velocity from matching the line-centre shifts seen by HIFI (see Sect. 3.2). The parameters used in the calculation of the $H_2^{16}O$ models are listed in Table 4. The line profiles computed for different values of the turbulence velocity are compared to the line shapes observed by HIFI in Fig. 4. The values of the turbulence velocity that best match the shift seen for ortho-$H_2^{16}O$ and para-H_2O are 0.8 and 0.6 km s^{-1}, respectively. Although the difference in the derived turbulence velocity is small (~0.2 km s^{-1}), the high-quality HIFI data seems to suggest that the main line-formation region for the o-H_2O lines has a slightly different turbulence velocity than for p-H_2O. However, as an uncertainty of 0.1 km s^{-1} in the turbulence velocity, propagates to an uncertainty of only 5% at most for the predicted line profiles, we adopt a value of 0.7 km s^{-1} for both spin isomers.

After fixing the turbulence velocity, we calculated the reduced-χ^2 of the fits to the PACS and HIFI line fluxes for models with different values of the ortho-$H_2^{16}O$ and para-$H_2^{16}O$ abundances. For ortho-$H_2^{16}O$, we get the best result for an abundance of 6×10^{-4} for both HIFI and PACS data. For para-$H_2^{16}O$, a value of 3×10^{-4} fits better the PACS data, while a value between 4×10^{-4} and 3×10^{-4} is the best match for the HIFI observations. Taking the whole dataset into account, the best fits for ortho- and para-$H_2^{16}O$ are achieved with abundances of $(6^{+3}_{-2}) \times 10^{-4}$ and $(3^{+2}_{-1}) \times 10^{-4}$, respectively. These models are compared to the lines observed by HIFI in Figs. 5 and 6 for ortho- and para-$H_2^{16}O$, respectively.

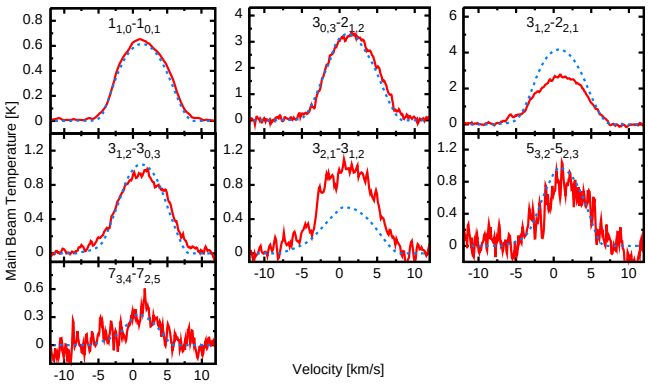

Fig. 5. Best fit model (dashed-blue line) to the ortho-$H_2^{16}O$ lines compared to the lines observed by HIFI (solid-red line). The model has an ortho-$H_2^{16}O$ abundance of 6×10^{-4} and a turbulence velocity of 0.7 km s^{-1}. The adopted value for the $\upsilon_{\rm LSR}$ of 40.4 km s^{-1} was subtracted from the observed lines.

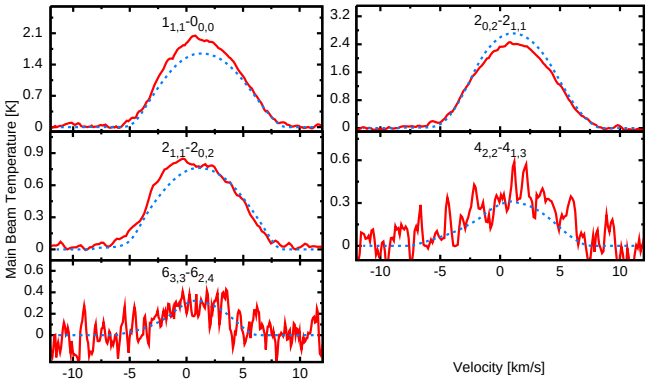

Fig. 6. Best fit model (dashed-blue line) to the para-$H_2^{16}O$ lines compared to the lines observed by HIFI (solid-red line). The model has a para-$H_2^{16}O$ abundance of 3×10^{-4} and a turbulence velocity of 0.7 km s^{-1}. The adopted value for the $\upsilon_{\rm LSR}$ of 40.4 km s^{-1} was subtracted from the observed lines.

4.1. H_2O Isotopologues

We calculated models for each of the four isotopologues of H_2O, ortho-$H_2^{17}O$ and $H_2^{18}O$ and para-$H_2^{17}O$ and $H_2^{18}O$, considering both a turbulence velocity of 0.7 km s^{-1} and different values for the abundance of each isotopologue. The optical depths of the transitions are considerably smaller than the corresponding ones of the main isotopologues, causing the derived abundances to be roughly independent of $\upsilon_{\rm turb}$. The uncertainty on $\upsilon_{\rm turb}$ propagates to an uncertainty of a few percent in the line fluxes of the rarer isotopologues.

The models are compared to the observations in Fig. 7 and the best abundance values of each isotopologue relative to H_2 are given in Table 5. The best models were selected by comparing the integrated line fluxes with the observations. Then, we computed the different isotopologic ratios given in Table 6, which allow us to derive the $^{16}O/^{17}O$, the $^{16}O/^{18}O$ isotopic ratios and the ortho-to-para ratio. We note, however, that the line shapes of the two ortho-H_2O isotopologues are not well repro-

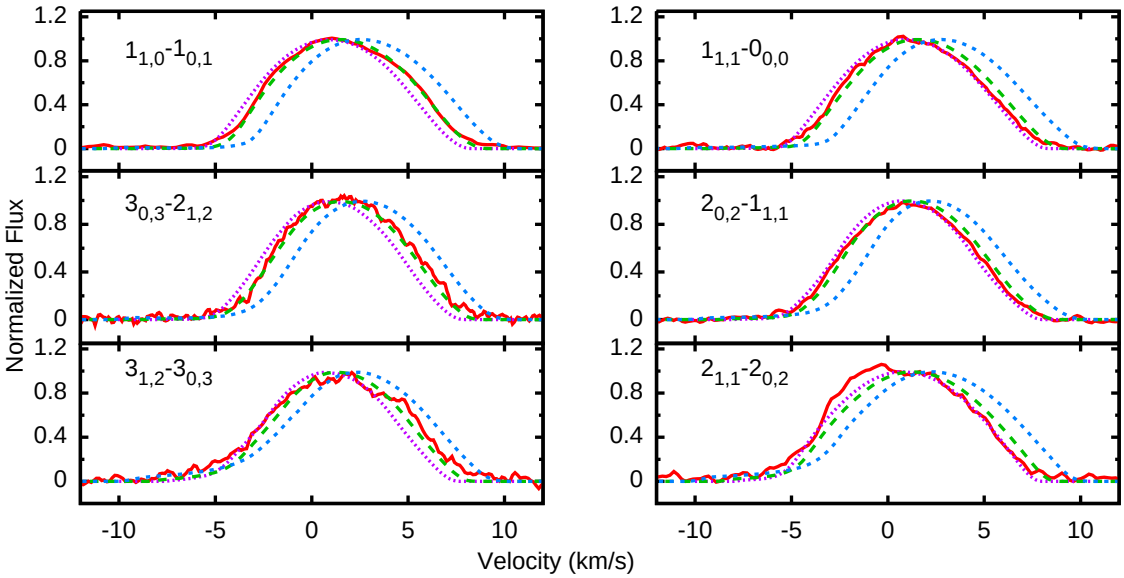

Fig. 4. Normalized profiles of ortho- and para-$H_2^{16}O$ transitions observed by HIFI compared to models with different values of the turbulence velocity and all other parameters kept fixed. The solid red line represents the data, and models with turbulence velocities of 0.5, 0.8 and 1.4 km s^{-1} are represented by dotted purple, long-dashed green and short-dashed blue lines, respectively. The adopted value for the $\upsilon_{\rm LSR}$ of 40.4 km s^{-1-1} was subtracted from the observed lines.

Table 5. Best fit results for the abundances of the isotopologues of H_2O. The super- and subscript give the 1-σ uncertainties in the determined values.

Molecule	Best
para-$H_2^{17}O$	$2^{+1}_{-1} \times 10^{-7}$
para-$H_2^{18}O$	$1.6^{+0.4}_{-0.6} \times 10^{-6}$
ortho-$H_2^{17}O$	$6^{+4}_{-2} \times 10^{-7}$
ortho-$H_2^{18}O$	$3^{+1}_{-1} \times 10^{-5}$

Table 6. Derived isotopologic ratios. The super and subscript give the 1-σ uncertainties in the determined values.

Molecules	Ratio $^{\rm upper\,limit}_{\rm lower\,limit}$
o-$H_2^{16}O$/o-$H_2^{17}O$	$1000\,^{+1200}_{-600}$
(o-$H_2^{16}O$/o-$H_2^{18}O$)	$20\,^{+25}_{-8}$
p-$H_2^{16}O$/p-$H_2^{17}O$	$1500\,^{+2500}_{-800}$
p-$H_2^{16}O$/p-$H_2^{18}O$	$190\,^{+210}_{-90}$
o-$H_2^{16}O$/p-$H_2^{16}O$	$2\,^{+2.5}_{-0.8}$
o-$H_2^{17}O$/p-$H_2^{17}O$	$3\,^{+7}_{-1.5}$
(o-$H_2^{18}O$/p-$H_2^{18}O$)	$19\,^{+21}_{-9}$
p-$H_2^{18}O$/p-$H_2^{17}O$	$8\,^{+12}_{-5}$
(o-$H_2^{18}O$/o-$H_2^{17}O$)	$50\,^{+50}_{-30}$

Notes. The ratios between parentheses were not considered when deriving the final values.

duced, particularly that of o-$H_2^{18}O$. The single observed line of o-$H_2^{18}O$ is shifted with respect to the modelled transitions and very high values of the o-$H_2{}^{18}O$ abundance are needed to predict the observed line strength. Therefore, the values derived for

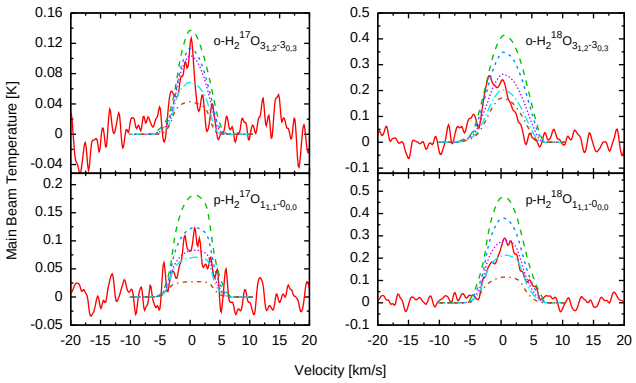

Fig. 7. The solid red line represents the HIFI data, the dashed green, short-dashed blue, dotted purple, dashed-dotted light-blue and short-dashed-dotted brown lines represent, respectively, models with abundances relatively to H_2 of: (4, 2, 1.2, 0.4, 0.2) $\times 10^{-6}$ for for ortho-$H_2^{17}O$; (1.2, 0.8, 0.4, 0.2, 0.12) $\times 10^{-4}$ for ortho-$H_2^{18}O$; (8, 4, 2, 1.2, 0.4) $\times 10^{-7}$ for para-$H_2^{17}O$; and (8, 4, 2, 1.2, 0.4) $\times 10^{6}$ for para-$H_2^{18}O$. We adopted a value of 0.7 km s^{-1} for the turbulence velocity in these calculations. The adopted value for the $\upsilon_{\rm LSR}$ of 40.4 km s^{-1} was subtracted from the observed lines.

the $^{16}O/^{18}O$ ratio and for the H_2O ortho-to-para ratio based on this line do not agree with those derived using any other pair of observed lines. Because of this mismatch, we have not included the values derived from the o-$H_2{}^{18}O$ line in the ortho-to-para and isotopic ratios calculations. Modifying the dissociation radius and turbulence velocity does not improve the fitting of this transition. Discarding the o-$H_2{}^{18}O$ line, we obtain: ortho-to-para = $2.5\,^{+2.5}_{-1.0}$, $^{16}O/^{17}O = 1250\,^{+750}_{-450}$ and $^{16}O/^{18}O = 190\,^{+210}_{-90}$ (see also Table 6).

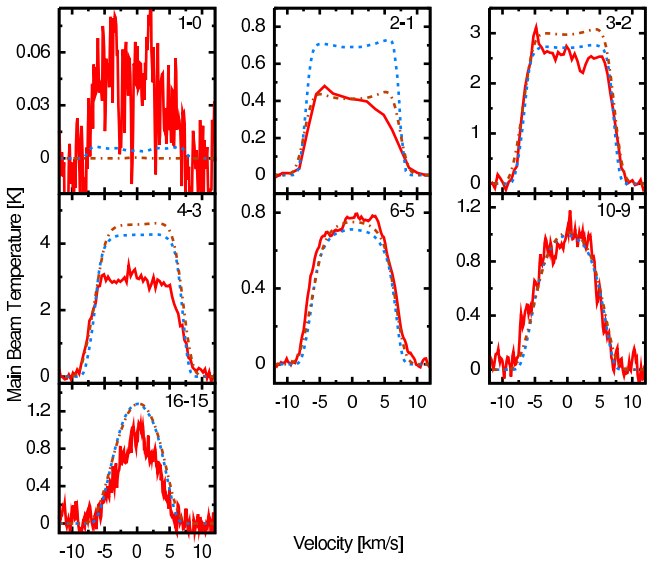

Fig. 8. A model for the ^{12}CO lines with $\upsilon_{\rm turb}$ = 0.7 km s^{-1} (short-dashed blue line) is compared to the best model found in Paper I ($\upsilon_{\rm turb}$ = 1.4 km s^{-1}; dotted-dashed brown line). The observed ^{12}CO lines are shown in red. The adopted value for the $\upsilon_{\rm LSR}$ of 40.4 km s^{-1} was subtracted from the observed lines. The lines J = 16 – 15, 10 – 9 and 6 – 5 were observed with HIFI, J = 4 – 3 and 3 – 2 with APEX, J = 2 – 1 with SMT and J = 1 – 0 with SEST.

4.2. Consequences of a lower $\upsilon_{\rm turb}$ for the ^{12}CO lines

The turbulence velocity that resulted from the ^{12}CO analysis in Paper I was 1.4 km s^{-1}. However, this value was not strongly constrained. Although this higher value is better at reproducing the ^{12}CO line wings, the differences between models for 0.6–0.8 and 1.4 km s^{-1} are small. In Fig. 8 we show a comparison between the ^{12}CO model from Paper I and a model with $\upsilon_{\rm turb}$ = 0.7 km s^{-1}. The change in the value of the turbulence velocity only has an impact on the total line flux of the transitions having $J_{\rm up}$ < 6, most notably that of J = 2 – 1. When a lower value of the turbulence velocity is used, the model predictions for the J = 1 – 0 and 2 – 1 transitions get somewhat stronger, while those for the 3 – 2 to 6 – 5 transitions get somewhat weaker. The emission from line J = 2 – 1 could be decreased by considering an even smaller ^{12}CO dissociation radius than the one obtained in Paper I, but this will not resolve the discrepancy in the J = 1 – 0 line. The poor fit to the second line is the main shortcoming of our ^{12}CO model. We conclude that a lower value for the turbulence velocity does not affect significantly the quality of our fit, except for the very low-excitation lines J = 2 – 1 and J = 1 – 0, the second of which was also poorly reproduced by our original ^{12}CO model. Furthermore, we can expect the turbulence velocity to be different in the formation regions of $H_2^{16}O$ and ^{28}SiO and of the low-excitation ^{12}CO lines, since the ^{12}CO envelope is significantly larger than that of $H_2^{16}O$ and ^{28}SiO. However, since it is not possible to determine a precise value for the turbulence velocity from the ^{12}CO lines, we cannot draw any conclusion on changes in this parameter between the $H_2^{16}O$ and ^{28}SiO envelopes and the ^{12}CO outer envelope.

4.3. Reproducing the PACS spectrum

In Fig. 9, we compare our ^{12}CO and ortho- and para-$H_2^{16}O$ models to the PACS spectrum of W Hya. The ^{28}SiO lines modelled do not contribute significantly to the PACS spectrum and were not included in the plot. The vast majority of the prominent lines seen in the spectrum can be accounted for by our $H_2^{16}O$ model. A small fraction of the strong lines, however, is not predicted. These lines have peaks around 61.52, 72.84, 78.47, 79.12, 86.52, 89.78, 154.88 and 163.12 μm. The lines observed at 79.12 and 163.12 μm can be associated with OH transitions (Sylvester et al. 1997). Those at 78.47, 86.52 and 89.78 μm might be explained by ^{28}SiO maser emission (Decin et al., *in prep.*). We were not able to identify the lines observed at 61.52, 72.84 and 154.88 μm.

5. Model for gas-phase ^{28}SiO emission

In Paper I, we assumed a standard value for the ^{12}CO abundance relative to H_2 of 4×10^{-4}. Were all carbon and silicon used to form ^{12}CO and ^{28}SiO, respectively, and solar composition assumed, then the ^{12}CO-to-^{28}SiO abundance ratio would be roughly 8.3, corresponding to an ^{28}SiO photospheric abundance of 4.8×10^{-5}.

In order to establish the location in the outflow where silicate dust particles condense, and the fraction of the ^{28}SiO that is converted from the molecular phase to the solid phase in the inner wind, we modelled the ^{28}SiO line emission detected by *Herschel*. The broad spectral coverage of PACS and SPIRE provides a series of lines with upper-level energies ranging from 137 to 1462 K above the ground state, covering the region where silicates are expected to condense (Gail & Sedlmayr 1999) and, consequently, where a decrease in the ^{28}SiO abundance should be seen.

We compare these data to a grid of models in which the photospheric ^{28}SiO abundance relative to H_2, $f_{\rm SiO}^{\circ}$, the condensation fraction of ^{28}SiO in solid material, $f_{\rm cond}$, and radius at which this happens, $R_{\rm cond}$, are varied. For $f_{\rm SiO}^{\circ}$ we apply (10, 8, 6, 5, 4, 2) $\times 10^{-5}$. For $f_{\rm cond}$ we adopt 0, 0.35, 0.65, and 0.90. The first value implies no condensation of solids. For each of the abundance profiles in which condensation was considered, we take $R_{\rm cond}$ to be either 5, 10, or 20 $R_\star$. This adds up to a total of sixty models. We note that models without condensation are equivalent to models with a high ^{28}SiO abundance in which condensation occurs deep in the envelope, at about 2 $R_\star$, as our models are not sensitive to the abundance at radii smaller than about 5 $R_\star$. To give an example, a model with an initial abundance of 4×10^{-5} is analogous to a model with $f_{\rm SiO}^{\circ} = 6 \times 10^{-5}$ and $f_{\rm cond}$ = 0.33 in which condensation occurs close to the star.

As shown in Table 7, the models were ranked based on the calculated reduced-χ^2 fit to the line fluxes obtained with SPIRE, HIFI and PACS, listed in Table B.1 of the appendix. The ten best models have ^{28}SiO abundances between 2.5 $\times 10^{-5}$ and 4.0 $\times 10^{-5}$ relative to H_2 in the region between 10 and 100 $R_\star$, i.e. in the region where the ^{28}SiO emission originates (see Fig. 1). The condensation radius of ^{28}SiO is not strongly constrained. However, condensation at 10 $R_\star$ or less seems preferred over condensation at 20 $R_\star$. In the top-fifteen-ranked models, those with a condensation fraction of 0.65 all have higher photospheric ^{28}SiO abundance than expected on the basis of a solar carbon-to-silicon ratio. If the photospheric ^{28}SiO abundance is assumed to be solar ($f_{\circ}^{\rm SiO}$ between 4.0 and 6.0 $\times 10^{-5}$), a condensation fraction of 0.35 or less is preferred. Furthermore, the slope seen in Fig. 10 for the observed line fluxes distribution in terms of J is

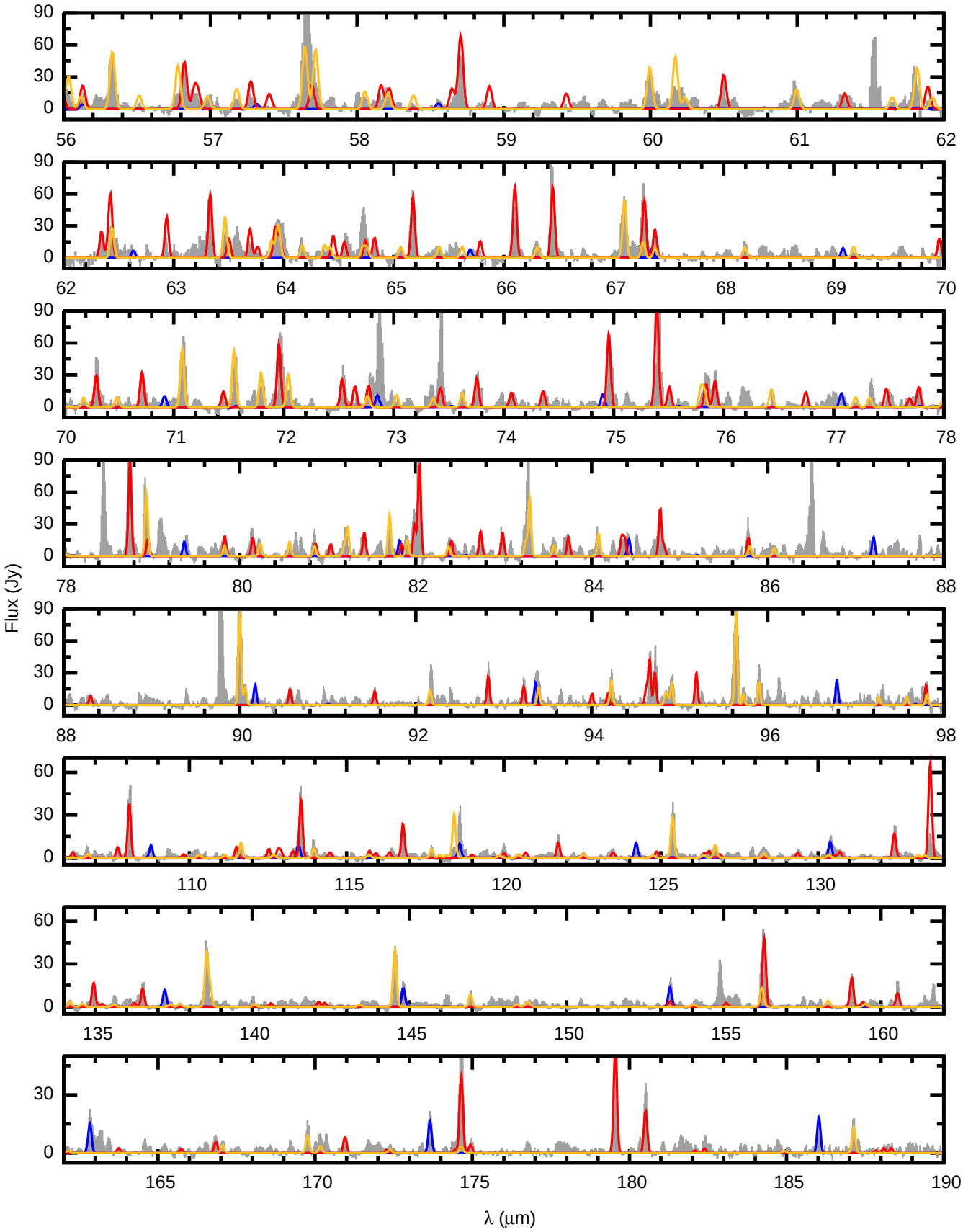

Fig. 9. The PACS spectrum (represented by the grey-filled histogram) is compared to our best model, with the parameters given in Table 1 but with $\upsilon_{\rm turb}$ of 0.7 km s^{-1} and with ortho- and para-$H_2^{16}O$ abundances of 6×10^{-4} and 3×10^{-4}, respectively. The ^{12}CO model is shown by the full-blue line, the ortho-$H_2^{16}O$, by the full-red line and the para-$H_2^{16}O$, by the full-yellow line.

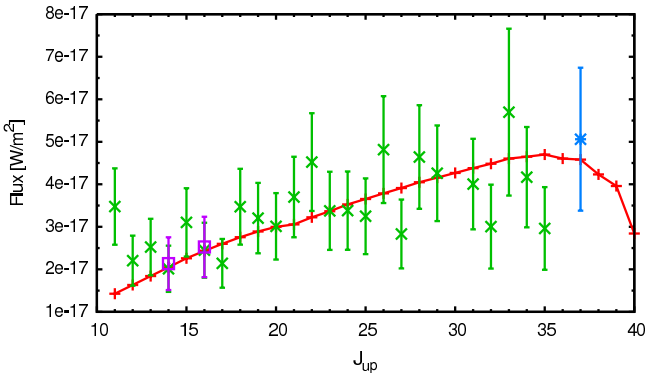

Fig. 10. The best model for the ^{28}SiO line emission (red line and crosses), with $f_{\circ}^{\rm SiO} = 4 \times 10^{-5}$ and $f_{\rm cond} = 0$, is compared to the line fluxes observed by SPIRE (green), PACS (blue) and HIFI (purple).

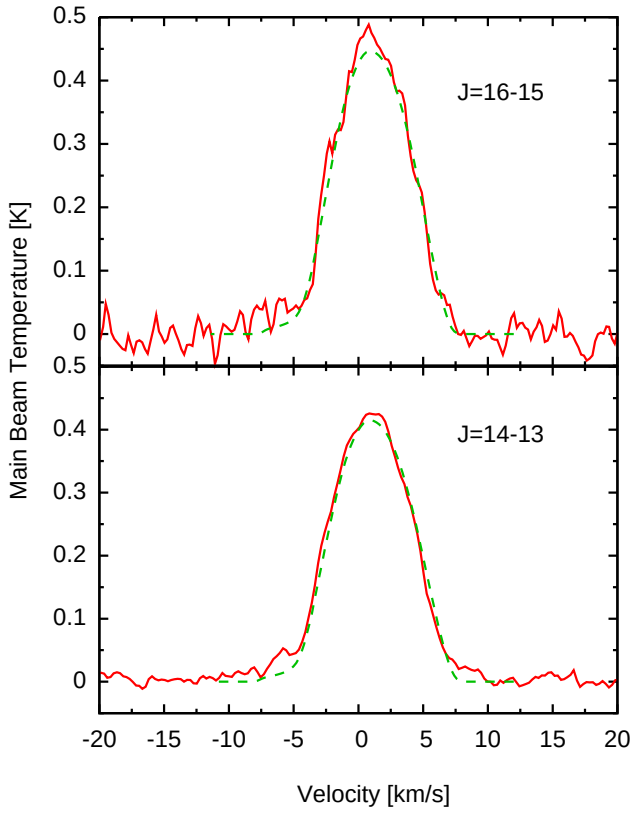

Fig. 11. The best ^{28}SiO model (green-dashed line) is compared to the line shapes observed by HIFI (solid red line). The adopted value for the $\upsilon_{\rm LSR}$ of 40.4 km s^{-1} was subtracted from the observed lines.

much better reproduced by models with no or very little condensation.

The fit to the $J = 14-13$ and $16-15$ ^{28}SiO lines observed by HIFI, shown in Fig. 11, is consistent with $\upsilon_{\rm turb} = 0.7 \pm 0.1$ km s^{-1}.

Table 7. Calculated reduced-χ^2 of the fit to the line fluxes of the set of ^{28}SiO lines listed in Table B.1 of the appendix. The models are listed in order of fit quality, with the best fit at the top.

$f_{\rm SiO}^{\circ}/10^{-5}$	$f_{\rm cond}$	$R_{\rm cond}$ [$R_\star$]	red-χ^2
4.0	0	-	1.08
6.0	0.35	5	1.11
10.0	0.65	5	1.18
5.0	0	-	1.20
5.0	0.35	5	1.23
8.0	0.35	5	1.29
6.0	0.35	10	1.30
5.0	0.35	10	1.35
5.0	0.35	20	1.38
4.0	0.35	20	1.40
8.0	0.65	5	1.44
6.0	0	-	1.55
6.0	0.35	20	1.55
4.0	0.35	5	1.57
4.0	0.35	10	1.59
8.0	0.35	10	1.60
10.0	0.65	10	1.72
8.0	0.65	10	1.78
10.0	0.35	5	1.82
5.0	0.65	20	1.84
4.0	0.65	20	1.91
6.0	0.65	20	1.92
6.0	0.65	5	2.03
6.0	0.65	10	2.07
2.0	0	-	2.19
10.0	0.35	10	2.21
8.0	0.35	20	2.25
5.0	0.65	10	2.35
8.0	0.65	20	2.39
5.0	0.65	5	2.51
5.0	0.90	20	2.58
4.0	0.90	20	2.59
2.0	0.35	20	2.62
8.0	0	-	2.66
6.0	0.90	20	2.70
4.0	0.65	10	2.76
10.0	0.65	20	3.06
2.0	0.65	20	3.08
2.0	0.35	10	3.15
8.0	0.90	20	3.16
4.0	0.65	5	3.17
10.0	0.35	20	3.25
2.0	0.35	5	3.46
2.0	0.90	20	3.51
10.0	0.90	10	3.65
10.0	0.90	20	3.77
8.0	0.90	10	3.93
10.0	0	-	4.15
10.0	0.90	5	4.16
6.0	0.90	10	4.32
2.0	0.65	10	4.43
5.0	0.90	10	4.58
8.0	0.90	5	4.87
4.0	0.90	10	4.93
2.0	0.65	5	5.48
6.0	0.90	5	5.79
2.0	0.90	10	6.15
5.0	0.90	5	6.36
4.0	0.90	5	7.04
2.0	0.90	5	8.95

6. Discussion

6.1. The turbulence velocity

The turbulence velocity probed by a given line is that of the region where the line is excited and from which photons can escape. The lines observed by HIFI for the ortho- and para-$H_2^{16}O$ transitions have similar excitation energies, hence they may be expected to form in a similar part of the outflow if the spin isomers themselves occupy the same region.

We found a small difference in the turbulent velocity value that predicts best the observed line shapes of the ortho- and para-H_2O, 0.8 km s^{-1} and 0.6 km s^{-1} respectively. The $\upsilon_{\rm turb}$ derived by Khouri et al. (2014) based on the ^{12}CO line shapes was 1.4 ± 1.0 km s^{-1}. Since the low-excitation CO lines probe the outer parts of the wind, this could be another indication of a turbulent velocity gradient. However, the uncertainty in the $\upsilon_{\rm turb}$ values from CO are sizable. Moreover, the observed line shapes of both H_2O spin isomers are not perfectly fitted for any value of $\upsilon_{\rm turb}$. Although these diagnostics suggest a gradient, GASTRoNOoM can only calculate models with a constant turbulent velocity and therefore we cannot test this possibility at the moment. We adopt $\upsilon_{\rm turb} = 0.7 \pm 0.1$ km s^{-1}.

Maercker et al. (2009) found the dissociation radius and the shape of the abundance profile to also have an impact on the line shapes. We discuss our assumptions for these properties in Section 3.1. We have tested the impact of decreasing the dissociation radius on the line shapes. The lines become narrower, the red-wing being more strongly affected. The dissociation radii and the abundance profile have an impact on the line shapes and their peak position and add to the uncertainty on the determined turbulence velocity. However, if the abundance profile of ortho- and para-$H_2^{16}O$ are similar, there should be no relative difference between the line shapes of the two spin isomers.

6.2. Isotopic ratios and evolutionary status of W Hya

During the evolution of low- and intermediate-mass stars leading up to the AGB and on the AGB, the abundances of the two minor oxygen isotopes are expected to vary considerably, especially due to the first- and third-dredge-up events. The effect of the first-dredge-up on the ^{16}O/^{17}O surface isotopic ratio is found to depend quite sensitively on the initial stellar mass, the values of this ratio after this first-dredge-up event is a steeply decreasing function of stellar mass for stars with main sequence mass between 1 and 3 $M_\odot$ (e.g. Boothroyd et al. 1994; Lattanzio & Boothroyd 1997; Palmerini et al. 2011; Charbonnel & Lagarde 2010). During the third-dredge-up, the surface oxygen isotopic ratios are expected to change only if hot bottom burning is active (e.g. Busso et al. 1999; Charbonnel & Lagarde 2010; Karakas 2011). In this case, the abundance of ^{18}O drops strongly while that of ^{17}O remains almost unchanged. Justtanont et al. (2013) recently lend support to this prediction by presenting observations that clearly show that the abundance of $H_2{}^{17}O$ is considerably higher than that of $H_2{}^{18}O$ for a set of OH/IR stars observed with HIFI.

The isotopic ratios determined for W Hya, ^{16}O/^{17}O = 1250^{+750}_{-450} and ^{16}O/^{18}O = 190^{+210}_{-90}, are lower than the solar values of $(^{16}O/^{17}O)_\odot = 2600$ and $(^{16}O/^{18}O)_\odot = 500$. The observed value of 1250 implies that W Hya had an initial mass of about 1.5 $M_\odot$. Evolutionary models show the ^{16}O/^{17}O ratio after the first dredge-up to be independent of metallicity. Since the ^{16}O/^{17}O surface ratio is such a steep function of initial mass, the initial mass of W Hya would be constrained to be within 1.3 and 1.7 $M_\odot$. Such a star would reach the AGB phase in about 3 gigayears. If W Hya has less metals than the Sun, the determined value for the ^{16}O/^{17}O surface ratio would also be consistent with it having an initial mass of more than 4 $M_\odot$. It is unlikely, however, that W Hya is either metal-poorer than the Sun or so massive.

The value for the ^{16}O/^{18}O ratio does not agree with what is found with available evolutionary models. The observed value of 190 is lower than that of the Sun. All models predict this ratio to be a weak function of mass and to increase during evolution, therefore the observed value cannot be reconciled with predictions. Interestingly, Decin et al. (2010b) determine the ^{16}O/^{18}O ratio of the also oxygen-rich AGB star IK Tau to be 200, a value that is very close to the value determined by us for W Hya.

One solution to this problem may be that both W Hya and IK Tau are richer in metals than the Sun, since the ^{16}O/^{18}O ratio is expected to be inversely proportional to metal content (Timmes et al. 1995). The observed isotopic ratio then requires that W Hya and IK Tau are about twice as rich in metals than is the Sun. If that is not the case, and the low ^{16}O/^{18}O ratio is confirmed for these two objects, our findings would imply that the evolution of the ^{18}O surface abundance up to the AGB stage is not yet well understood. However, the uncertainty associated with the ^{16}O/^{18}O measurement does not allow one to draw a firm conclusion on this matter at the moment.

6.3. ^{28}SiO condensation

If we consider a photospheric ^{28}SiO abundance expected for solar composition ($f_\circ^{\rm SiO} = 4.8 \times 10^{-5}$), a dust mass-loss rate of $2.8 \times 10^{-10} M_\odot$yr^{-1} and the silicon-bearing grains to consist of olivine silicates ($MgFeSiO_4$) (see Paper I), our model requires about one-third of the silicon atoms in the wind of W Hya to be in dust grains. We thus expect to see a decrease in the ^{28}SiO abundance from 4.8×10^{-5} to 3.2×10^{-5} over the region where silicates condense. Furthermore, our dust model predicts that silicates are formed in W Hya's wind as close as ~5 stellar radii (or 10 AU) to the surface. Observations carried out by Zhao-Geisler et al. (2011) with MIDI/VLTI set a lower limit on the silicate formation radius at 28 photospheric radii (equivalent to 50 AU or 0.5 arcsec). That corresponds to 22 $R_\star$ (equivalent to ~ 40 AU) in our model, when we correct for the different distance adopted by them. Furthermore, aperture-masked polarimetric interferometry observations carried out by Norris et al. (2012) reveal a close-in halo of large transparent grains in W Hya. The composition of the grains could not be determined, but if this material also contains silicon it has to be considered in the silicon budget.

Our molecular-line-emission calculations indicate that ^{28}SiO does not suffer from strong depletion in W Hya's wind. Furthermore, an ^{28}SiO abundance of $(3.3\pm0.8)\times10^{-5}$ between 10 and 100 $R_\star$ is required in order to reproduce the observed ^{28}SiO lines. Adding to that the silicon that is in our dust model, which corresponds to an abundance of 1.6×10^{-5}, we reach a total silicon abundance of 4.9×10^{-5}. This is very close to the abundance expected based on a solar silicon-to-carbon ratio, i.e. 4.8×10^{-5} for ^{28}SiO. Models with condensation occurring at radii equal to, or smaller than, 10 stellar radii are preferred to those with condensation at 20 stellar radii but we are not able to determine the condensation radius based in our data. One could expect condensation to happen over a few or even tens of stellar radii, a scenario not explored in our calculations. Despite the good agreement regarding the silicon budget, we note that our dust model was based on the one obtained by Justtanont et al. (2005) and

that we have not studied the dust envelope in detail, as considering different dust species and/or distribution. Furthermore, the present dust model does not agree with the observations carried out by Zhao-Geisler et al. (2011), which show that silicates do not condense closer than about 40 AU. We will analyse in depth the dust envelope of W Hya under the light of the gas-phase wind model presented here in an upcoming study.

Regarding the outer ^{28}SiO envelope, González Delgado et al. (2003) modelled the ^{28}SiO pure rotational emission of the ground-vibrational state and obtained an ^{28}SiO abundance of 1.5×10^{-5}. The authors, however, studied the ^{28}SiO abundance relative to ^{12}CO mainly in a statistical way. They compared their models to low-excitation transitions, $J = 2-1$, $3-2$, $5-4$ and $6-5$, which trace mostly the outer parts of the ^{28}SiO envelope. The value González Delgado et al. (2003) derive for the ^{28}SiO abundance is a factor of two lower than the 3.3×10^{-5} abundance found by us. However, if the lower mass-loss rate, 8×10^{-8} and the smaller distance, 65 parsecs, considered by them are taken into account the derived abundance should be even smaller, in the context of our model. Our calculations overpredict the emission seen in these low-excitation transitions by a factor of four, consistent with the difference in the abundances that are obtained. Lucas et al. (1992) determined the half-intensity angular radius for the ^{28}SiO transition $J = 2-1$ to be 0.9 ± 0.1 arcseconds. This value is substantially smaller than the value derived by González Delgado et al. (2003) for the *e*-folding radius of the ^{28}SiO abundance, 2.4×10^{15} cm or 2 arcseconds in the context of our model. The inconsistency is only apparent, as González Delgado et al. point out that these two radii are indeed expected to differ. The authors find that the *e*-folding radii determined by them are about three times larger than the half-intensity radius of the $J = 2-1$ ^{28}SiO transition for model envelopes. Schöier et al. (2004) observed the ^{28}SiO $J = 2-1$ transition of R Dor and L^2 Pup with the Australia Telescope Compact Array. By modelling the interferometric data, the authors found that the ^{28}SiO abundance is better described by a two-component profile, a high abundance ($f_{\rm SiO}\approx4\times10^{-5}$) inner component and a lower abundance ($f_{\rm SiO}\approx2-3\times10^{-6}$) extended component. The radius where the abundance drops is found to be between 1 and 3×10^{15} cm.

The low-excitation transitions probe mostly the outer envelope, where dissociation occurs. The population of level $J = 6$ of ^{28}SiO reaches its maximum at 60 R$_\star$ (1.5 arcseconds or 1.8×10^{15} cm in the context of our model). Therefore, the abundances derived based on transitions from $J = 6$ and lower levels will depend on the assumed dissociation profile. We have calculated models with smaller dissociation radii and shallower dissociation profiles. We have done so by decreasing, respectively, the value of the *e*-folding radius $r_{\rm e}$ and of the exponent p, initially kept at $p = 2$, in the expression for the ^{28}SiO abundance profile (see Equation 2). For reasonable values of these two parameters, the models are still unable to fit the low-excitation transitions. An alternative possibility to explain simultaneously the high- and low-excitation lines may be that ^{28}SiO suffers from further depletion from the gas-phase in-between the region where the lines observed by *Herschel* and those observed by SEST are excited. At such large distances from the star, however, condensation and dissociation are indistinguishable on the basis of ^{28}SiO line emission modelling. The $J_{\rm up} > 10$ lines modelled by us, are all produced closer to the star and, therefore, trace the depletion of ^{28}SiO independently of dissociation. Thanks to the apparent complex nature of the ^{28}SiO dissociation region and since the choice of dissociation radius does not have a significant impact on the derived value for the ^{28}SiO abundance, we do not attempt to fit the low-excitation ^{28}SiO lines in detail. The value for the ^{28}SiO depletion obtained by us is representative of the inner wind, for $r < 1.5\times10^{15}$ cm.

7. Summary

We present an analysis of the ortho-$H_2^{16}O$, para-$H_2^{16}O$, ortho-$H_2^{17}O$, para-$H_2^{17}O$, ortho-$H_2^{18}O$, para-$H_2^{18}O$ and $^{28}Si^{16}O$ emission from the wind of the nearby oxygen-rich AGB star W Hya, as measured by the three instruments on board *Herschel*. The work builds on the structure model of Khouri et al. (2014), derived on the basis of ^{12}CO lines, and is the first combined ^{12}CO, $H_2^{16}O$ and ^{28}SiO analysis of this source.

The original structure model poorly constrained the turbulence component of the velocity field in the outflow. $H_2^{16}O$ and ^{28}SiO lines put much firmer constraints on the value of the turbulence velocity, essentially because they are much optically thicker than the ^{12}CO lines. The presence of turbulence motions causes the H_2O and ^{28}SiO lines to shift to longer wavelengths, which, when compared to ^{12}CO profiles that form in roughly the same part of the wind appear to imply a blue-wing absorption. We find slightly different values for $\upsilon_{\rm turb}$ for ortho-$H_2^{16}O$ and para-$H_2^{16}O$, 0.8 and 0.6 km s^{-1} respectively, but as our code is not able to calculate models with a gradient in $\upsilon_{\rm turb}$, we have not explored this further.

The abundance of ortho-$H_2^{16}O$ and para-$H_2^{16}O$ relative to H_2 are $(6^{+3}_{-2})\times10^{-4}$ and $(3^{+2}_{-1})\times10^{-4}$. We also place constraints on the abundances of ortho-$H_2^{17}O$ and para-$H_2^{17}O$, and find an ortho-to-para ratio of $2.5^{+2.5}_{-1.0}$ – in agreement with the value of three expected for AGB stars. The $^{16}O/^{17}O$ ratio is found to be 1250^{+750}_{-450} and suggests that W Hya has an initial mass of about 1.5 M$_\odot$. We find an $^{16}O/^{18}O$ ratio of 190^{+210}_{-90}, which cannot be explained by the current generation of evolutionary models. It might be reconciled with predictions if W Hya is richer in metals than the Sun, but no firm conclusions can be drawn on this matter given the large uncertainties on the abundance determination.

We find an ^{28}SiO abundance between 10 and 100 R$_\star$ of $3.3\pm0.8\times10^{-5}$ relative to H_2. Adding to this gas-phase abundance the abundance needed by our dust model, equivalent to 1.6×10^{-5}, we can account for all silicon in the wind of W Hya if a solar silicon-to-carbon ratio is assumed.

Acknowledgements. HIFI has been designed and built by a consortium of institutes and university departments from across Europe, Canada, and the United States under the leadership of SRON Netherlands Institute for Space Research, Groningen, The Netherlands and with major contributions from Germany, France, and the US. Consortium members are Canada: CSA, U. Waterloo; France: CESR, LAB, LERMA, IRAM; Germany: KOSMA, MPIfR, MPS; Ireland, NUI Maynooth; Italy: ASI, IFSI-INAF, Osservatorio Astrofisico di Arcetri-INAF; Netherlands: SRON, TUD; Poland: CAMK, CBK; Spain: Observatorio Astronómico Nacional (IGN), Centro de Astrobiología (CSIC-INTA). Sweden: Chalmers University of Technology MC2, RSS & GARD; Onsala Space Observatory; Swedish National Space Board, Stockholm University SStockholm Observatory; Switzerland: ETH Zurich, FHNW; USA: Caltech, JPL, NHSC. PACS has been developed by a consortium of institutes led by MPE (Germany) and including UVIE (Austria); KUL, CSL, IMEC (Belgium); CEA, OAMP (France); MPIA (Germany); IFSI, OAP/AOT, OAA/CAISMI, LENS, SISSA (Italy); IAC (Spain). This development has been supported by the funding agencies BMVIT (Austria), ESA-PRODEX (Belgium), CEA/CNES (France), DLR (Germany), ASI (Italy), and CICYT/MCYT (Spain). SPIRE has been developed by a consortium of institutes led by Cardiff Univ. (UK) and including Univ. Lethbridge (Canada); NAOC (China); CEA, LAM (France); IFSI, Univ. Padua (Italy); IAC (Spain); Stockholm Observatory (Sweden); Imperial College London, RAL, UCL-MSSL, UKATC, Univ. Sussex (UK); Caltech, JPL, NHSC, Univ. Colorado (USA). This development has been supported by national funding agencies: CSA

(Canada); NAOC (China); CEA, CNES, CNRS (France); ASI (Italy); MCINN (Spain); SNSB (Sweden); STFC (UK); and NASA (USA). HIFISTARS: *The physical and chemical properties of circumstellar environments around evolved stars*, (P.I. V. Bujarrabal, is a *Herschel*/HIFI guaranteed time key program (KPGT_vbujarra_1) devoted to the study of the warm gas and water vapour contents of the molecular envelopes around evolved stars: AGB stars, red super- and hyper-giants; and their descendants: pre-planetary nebulae, planetary nebulae, and yellow hyper-giants. HIFISTARS comprises 366 observations, totalling 11 186min of *Herschel*/HIFI telescope time. See http://hifistars.oan.es; and Key_Programmes.shtml and UserProvidedDataProducts.shtml in the Herschel web portal (http://herschel.esac.esa.int/) for additional details. T.Kh. gratefully acknowledges the support from NWO grant 614.000.903. F.K. is supported by the FWF project P23586 and the ffg ASAP project HIL. MSc and RSz acknowledge support by the National Science Center under grant (N 203 581040).

References

Barlow, M. J., Nguyen-Q-Rieu, Truong-Bach, et al. 1996, A&A, 315, L241
Begemann, B., Dorschner, J., Henning, T., et al. 1997, ApJ, 476, 199
Bieging, J. H., Shaked, S., & Gensheimer, P. D. 2000, ApJ, 543, 897
Bladh, S. & Höfner, S. 2012, A&A, 546, A76
Boothroyd, A. I., Sackmann, I.-J., & Wasserburg, G. J. 1994, ApJ, 430, L77
Bujarrabal, V., Planesas, P., Martin-Pintado, J., Gomez-Gonzalez, J., & del Romero, A. 1986, A&A, 162, 157
Busso, M., Gallino, R., & Wasserburg, G. J. 1999, ARA&A, 37, 239
Charbonnel, C. & Lagarde, N. 2010, A&A, 522, A10
Cherchneff, I. 2006, A&A, 456, 1001
Cox, N. L. J., Kerschbaum, F., van Marle, A.-J., et al. 2012, A&A, 537, A35
de Graauw, T., Helmich, F. P., Phillips, T. G., et al. 2010, A&A, 518, L6
Decin, L., De Beck, E., Brünken, S., et al. 2010a, A&A, 516, A69
Decin, L., Hony, S., de Koter, A., et al. 2006, A&A, 456, 549
Decin, L., Justtanont, K., De Beck, E., et al. 2010b, A&A, 521, L4
El Eid, M. F. 1994, A&A, 285, 915
Faure, A., Crimier, N., Ceccarelli, C., et al. 2007, A&A, 472, 1029
Gail, H.-P. & Sedlmayr, E. 1999, A&A, 347, 594
González Delgado, D., Olofsson, H., Kerschbaum, F., et al. 2003, A&A, 411, 123
Griffin, M. J., Abergel, A., Abreu, A., et al. 2010, A&A, 518, L3
Groenewegen, M. A. T. 1994, A&A, 290, 531
Groenewegen, M. A. T., Waelkens, C., Barlow, M. J., et al. 2011, A&A, 526, A162
Habing, H. J. & Olofsson, H., eds. 2003, Asymptotic Giant Branch Stars
Harwit, M. & Bergin, E. A. 2002, ApJ, 565, L105
Hawkins, G. W. 1990, A&A, 229, L5
Henning, T., Begemann, B., Mutschke, H., & Dorschner, J. 1995, A&AS, 112, 143
Höfner, S. 2008, A&A, 491, L1
Huggins, P. J. & Healy, A. P. 1986, ApJ, 304, 418
Iben, Jr., I. 1975, ApJ, 196, 525
Iben, Jr., I. & Renzini, A. 1983, ARA&A, 21, 271
Imai, H., Nakashima, J.-I., Deguchi, S., et al. 2010, PASJ, 62, 431
Justtanont, K., Bergman, P., Larsson, B., et al. 2005, A&A, 439, 627
Justtanont, K., de Jong, T., Tielens, A. G. G. M., Feuchtgruber, H., & Waters, L. B. F. M. 2004, A&A, 417, 625
Justtanont, K., Khouri, T., Maercker, M., et al. 2012, A&A, 537, A144
Justtanont, K., Teyssier, D., Barlow, M. J., et al. 2013, A&A, 556, A101
Justtanont, K. & Tielens, A. G. G. M. 1992, ApJ, 389, 400
Karakas, A. I. 2010, MNRAS, 403, 1413
Karakas, A. I. 2011, in Astronomical Society of the Pacific Conference Series, Vol. 445, Why Galaxies Care about AGB Stars II: Shining Examples and Common Inhabitants, ed. F. Kerschbaum, T. Lebzelter, & R. F. Wing, 3
Kessler, M. F., Steinz, J. A., Anderegg, M. E., et al. 1996, A&A, 315, L27
Khouri, T., de Koter, A., Decin, L., et al. 2014, A&A, 561, A5 (Paper I)
Knapp, G. R., Pourbaix, D., Platais, I., & Jorissen, A. 2003, A&A, 403, 993
Landre, V., Prantzos, N., Aguer, P., et al. 1990, A&A, 240, 85
Langhoff, S. R. & Bauschlicher, Jr., C. W. 1993, Chemical Physics Letters, 211, 305
Lattanzio, J. C. & Boothroyd, A. I. 1997, in American Institute of Physics Conference Series, Vol. 402, American Institute of Physics Conference Series, ed. T. J. Bernatowicz & E. Zinner, 85–114
Lombaert, R., Decin, L., de Koter, A., et al. 2013, A&A, 554, A142
Lucas, R., Bujarrabal, V., Guilloteau, S., et al. 1992, A&A, 262, 491
Maercker, M., Schöier, F. L., Olofsson, H., et al. 2009, A&A, 494, 243
Maercker, M., Schöier, F. L., Olofsson, H., Bergman, P., & Ramstedt, S. 2008, A&A, 479, 779
Mamon, G. A., Glassgold, A. E., & Huggins, P. J. 1988, ApJ, 328, 797
Matsuura, M., Yates, J. A., Barlow, M. J., et al. 2013, MNRAS
Melnick, G. J., Stauffer, J. R., Ashby, M. L. N., et al. 2000, ApJ, 539, L77
Menten, K., Bujarrabal, V., Alcolea, J., et al. 2010, in COSPAR Meeting, Vol. 38, 38th COSPAR Scientific Assembly, 2490
Min, M., Dullemond, C. P., Dominik, C., de Koter, A., & Hovenier, J. W. 2009, A&A, 497, 155
Netzer, N. & Knapp, G. R. 1987, ApJ, 323, 734
Neufeld, D. A., Chen, W., Melnick, G. J., et al. 1996, A&A, 315, L237
Nordh, H. L., von Schéele, F., Frisk, U., et al. 2003, A&A, 402, L21
Norris, B. R. M., Tuthill, P. G., Ireland, M. J., et al. 2012, Nature, 484, 220
Palmerini, S., La Cognata, M., Cristallo, S., & Busso, M. 2011, ApJ, 729, 3
Pilbratt, G. L., Riedinger, J. R., Passvogel, T., et al. 2010, A&A, 518, L1
Poglitsch, A., Waelkens, C., Geis, N., et al. 2010, A&A, 518, L2
Rothman, L. S., Gordon, I. E., Barbe, A., et al. 2009, J. Quant. Spec. Radiat. Transf., 110, 533
Schöier, F. L., Olofsson, H., Wong, T., Lindqvist, M., & Kerschbaum, F. 2004, A&A, 422, 651
Schöier, F. L., van der Tak, F. F. S., van Dishoeck, E. F., & Black, J. H. 2005, A&A, 432, 369
Sharp, C. M. & Huebner, W. F. 1990, ApJS, 72, 417
Stoesz, J. A. & Herwig, F. 2003, MNRAS, 340, 763
Sylvester, R. J., Barlow, M. J., Nguyen-Q-Rieu, et al. 1997, MNRAS, 291, L42
Timmes, F. X., Woosley, S. E., & Weaver, T. A. 1995, ApJS, 98, 617
Vlemmings, W. H. T., Humphreys, E. M. L., & Franco-Hernández, R. 2011, ApJ, 728, 149
Winters, J. M., Le Bertre, T., Jeong, K. S., Helling, C., & Sedlmayr, E. 2000, A&A, 361, 641
Woitke, P. 2006, A&A, 460, L9
Zhao-Geisler, R., Quirrenbach, A., Köhler, R., Lopez, B., & Leinert, C. 2011, A&A, 530, A120
Zubko, V. & Elitzur, M. 2000, ApJ, 544, L137

Appendix A: Molecular models

When modelling the $H_2^{16}O$ transitions for all isotopologues, we include the 45 lowest levels of the ground and first vibrational states (i.e. the bending mode $\nu_2 = 1$ at 6.3 μm). For the two spin isomers of the main isotopologue, we have also included excitation to the first excited vibrational state of the asymmetric stretching mode ($\nu_3 = 1$). The difference on the model line fluxes due to the inclusion of the $\nu_3 = 1$ level is found to be 20% at maximum (Decin et al. 2010a). The frequencies, level energies and Einstein A coefficients were retrieved from the HITRAN $H_2^{16}O$ line list (Rothman et al. 2009). The collisional rates between $H_2^{16}O$ and H_2 were extracted from Faure et al. (2007).

Following Decin et al. (2010a), we consider the 40 lowest rotational levels of the ground and first vibrationally excited states when modelling the ^{28}SiO transitions. The Einstein A coefficients, energy levels and frequencies were taken from Langhoff & Bauschlicher (1993). The collisional rates between ^{28}SiO and H_2 were retrieved from the LAMBDA-database (Schöier et al. 2005).

Appendix B: Observed ^{28}SiO and $H_2^{16}O$ line fluxes

Table B.1. Integrated line fluxes and uncertainties for the ^{28}SiO transitions observed with *Herschel* for W Hya. The column *Instr.* lists the spectrograph used: HIFI, PACS, or SPIRE.

J_{up}	ν_0 [GHz]	*Instr.*	E [K]	Flux [10^{-17} W m^{-2}]
11	477.50	S	137.5	3.5 ± 0.7
12	520.88	S	162.5	2.2 ± 0.5
13	564.25	S	189.6	2.5 ± 0.5
14	607.61	S	218.8	2.0 ± 0.5
14	607.61	H	218.8	2.1 ± 0.4
15	650.96	S	250.0	3.1 ± 0.7
16	694.29	S	283.3	2.4 ± 0.5
16	694.29	H	283.3	2.5 ± 0.5
17	737.62	S	318.7	2.1 ± 0.5
18	780.93	S	356.2	3.5 ± 0.7
19	824.24	S	395.8	3.2 ± 0.7
20	867.52	S	437.4	3.0 ± 0.7
21	910.80	S	481.1	3.7 ± 0.8
22	954.05	S	526.9	4.5 ± 0.9
23	997.30	S	574.8	3.4 ± 0.8
24	1040.52	S	624.7	3.4 ± 0.8
25	1083.73	S	676.7	3.2 ± 0.7
26	1126.92	S	730.8	4.8 ± 1.0
27	1170.09	S	787.0	2.8 ± 0.7
28	1213.25	S	845.2	4.6 ± 1.0
29	1256.38	S	905.5	4.3 ± 0.9
31	1342.58	S	1032.3	4.0 ± 0.9
32	1385.65	S	1098.8	3.0 ± 0.9
33	1428.69	S	1167.4	5.7 ± 1.8
34	1471.72	S	1238.0	4.2 ± 1.0
35	1514.71	S	1310.7	3.0 ± 0.9
37	1600.63	P	1462.3	5.1 ± 1.5

Table B.2. Extracted ortho-$H_2^{16}O$ lines from the PACS observations. In the fifth column, we indicate if the line was flagged as a blend. We have specified if the blend happens with a known ortho- or para-$H_2^{16}O$ transition using, respectively, the superscripts ^{o} and ^{p}. Lines that were excluded due to masering happening in any of the models are identified by the superscript ^{m}.

Band	λ [μm]	E_{up} [K]	Transition ν, $J_{Ka,Kc} - J_{Ka,Kc}$	Blend -	Central λ of fit [μm]	Flux [W m^{-2}]	Error [W m^{-2}]	FWHM [μm]	PACS FWHM [μm]	Ratio -
B2A	56.816	1324.0	$\nu = 0, 9_{0,9} - 8_{1,8}$	No	56.814	1.48e-15	4.0e-16	0.040	0.039	1.034
	57.268	3614.8	$\nu = 1, 9_{0,9} - 8_{1,8}$	No	57.271	6.51e-16	3.0e-16	0.041	0.039	1.057
	57.684	5853.5	$\nu = 2, 9_{1,9} - 8_{0,8}$	Yes^{p}	57.660	6.76e-15	1.4e-15	0.063	0.039	1.602
	58.699	550.4	$\nu = 0, 4_{3,2} - 3_{2,1}$	No	58.706	1.96e-15	4.1e-16	0.040	0.039	1.029
	60.492	2744.8	$\nu = 1, 3_{3,0} - 2_{2,1}$	No	60.493	4.93e-16	1.7e-16	0.026	0.039	0.650
	62.335	3109.8	$\nu = 1, 6_{2,5} - 5_{1,4}$	No	62.340	4.55e-16	1.7e-16	0.043	0.039	1.085
	62.397	3673.2	$\nu = 1, 6_{5,2} - 7_{2,5}$	Yes^{o,p}	62.426	5.29e-16	1.9e-16	0.029	0.039	0.748
	62.418	1845.9	$\nu = 0, 9_{3,6} - 8_{4,5}$	Yes^{o,p}	62.426	5.29e-16	1.9e-16	0.029	0.039	0.748
	62.928	1552.6	$\nu = 0, 9_{1,8} - 9_{0,9}$	No	62.930	2.86e-16	1.3e-16	0.023	0.039	0.583
	63.324	1070.7	$\nu = 0, 8_{1,8} - 7_{0,7}$	No	63.320	1.72e-15	3.8e-16	0.044	0.039	1.107
	63.685	3363.5	$\nu = 1, 8_{1,8} - 7_{0,7}$	No	63.690	3.77e-16	1.6e-16	0.038	0.039	0.974
	63.914	1503.7	$\nu = 0, 6_{6,1} - 6_{5,2}$	Yes^{o,p}	63.940	1.38e-15	4.7e-16	0.057	0.039	1.458
	63.955	1749.9	$\nu = 7, 6_{1,0} - 5_{2,0}$	Yes^{o,p}	63.940	1.38e-15	4.7e-16	0.057	0.039	1.458
	65.166	795.5	$\nu = 0, 6_{2,5} - 5_{1,4}$	No	65.172	1.55e-15	3.3e-16	0.038	0.039	0.957
	66.093	1013.2	$\nu = 0, 7_{1,6} - 6_{2,5}$	No	66.101	1.18e-15	2.7e-16	0.039	0.039	0.999
	66.438	410.7	$\nu = 0, 3_{3,0} - 2_{2,1}$	No	66.440	2.07e-15	4.3e-16	0.036	0.039	0.915
	67.269	519.1	$\nu = 0, 3_{3,0} - 3_{0,3}$	Yes	67.272	2.26e-15	4.7e-16	0.052	0.039	1.322
	67.365	3323.3	$\nu = 1, 7_{1,6} - 6_{2,5}$	Yes	67.373	5.89e-16	1.7e-16	0.055	0.039	1.391
	70.287	2617.7	$\nu = 1, 3_{2,1} - 2_{1,2}$	No	70.287	8.53e-16	2.5e-16	0.031	0.039	0.799
	70.703	1274.2	$\nu = 0, 8_{2,7} - 8_{1,8}$	No	70.702	8.57e-16	2.0e-16	0.042	0.039	1.065
	71.947	843.5	$\nu = 0, 7_{0,7} - 6_{1,6}$	No	71.956	1.60e-15	3.4e-16	0.039	0.039	0.986
B2B	72.522	3137.6	$\nu = 1, 7_{0,7} - 6_{1,6}$	No	72.543	6.40e-16	1.6e-16	0.036	0.039	0.924
	73.415	5800.0	$\nu = 2, 8_{1,7} - 8_{0,8}$	No^{m}	73.431	2.02e-15	4.2e-16	0.029	0.039	0.743
	73.745	2745.3	$\nu = 1, 4_{2,3} - 3_{1,2}$	No	73.763	6.24e-16	1.8e-16	0.040	0.039	1.021
	74.945	1125.8	$\nu = 0, 7_{2,5} - 6_{3,4}$	Yes	74.966	1.64e-15	3.6e-16	0.054	0.039	1.374
	75.381	305.3	$\nu = 0, 3_{2,1} - 2_{1,2}$	No	75.407	3.51e-15	7.1e-16	0.031	0.039	0.783
	75.830	1278.6	$\nu = 0, 6_{5,2} - 6_{4,3}$	Yes^{p}	75.847	1.01e-15	2.7e-16	0.063	0.039	1.621
	75.910	1067.7	$\nu = 0, 5_{5,0} - 5_{4,1}$	No	75.923	5.62e-16	1.7e-16	0.031	0.039	0.805
	77.761	1524.9	$\nu = 0, 7_{5,2} - 7_{4,3}$	No	77.785	2.91e-16	8.1e-17	0.032	0.039	0.827
	78.742	432.2	$\nu = 0, 4_{2,3} - 3_{1,2}$	No	78.766	2.97e-15	6.0e-16	0.039	0.039	1.019
	78.946	3450.9	$\nu = 1, 6_{4,3} - 6_{3,4}$	Yes^{p}	78.950	1.41e-15	3.0e-16	0.042	0.039	1.078
	79.819	5358.0	$\nu = 2, 6_{1,5} - 5_{2,4}$	Yes	79.833	4.01e-16	1.3e-16	0.054	0.039	1.398
	80.139	3064.2	$\nu = 1, 4_{4,1} - 4_{3,2}$	Yes	80.157	6.18e-16	1.6e-16	0.051	0.038	1.323
	81.405	1729.4	$\nu = 0, 9_{2,7} - 9_{1,8}$	No	81.425	3.77e-16	1.1e-16	0.039	0.038	1.027
	82.031	643.5	$\nu = 0, 6_{1,6} - 5_{0,5}$	No	82.052	1.98e-15	4.1e-16	0.032	0.038	0.846
	82.726	3442.6	$\nu = 1, 7_{2,5} - 6_{3,4}$	No	82.757	3.51e-16	1.2e-16	0.042	0.038	1.116
	82.977	1447.6	$\nu = 0, 8_{3,6} - 8_{2,7}$	No	82.998	2.58e-16	9.2e-17	0.025	0.038	0.664
	83.724	5552.5	$\nu = 2, 7_{2,6} - 7_{1,7}$	Yes	83.737	5.00e-16	1.6e-16	0.064	0.038	1.690
	85.769	1615.4	$\nu = 0, 8_{4,5} - 8_{3,6}$	Yes^{p}	85.796	3.66e-16	8.9e-17	0.030	0.037	0.803
	92.811	1088.8	$\nu = 0, 6_{4,3} - 6_{3,4}$	No	92.826	4.43e-16	9.5e-17	0.034	0.035	0.967
	93.214	4838.3	$\nu = 2, 3_{2,2} - 2_{1,1}$	No	93.233	2.87e-16	6.6e-17	0.033	0.035	0.936
	94.644	795.5	$\nu = 0, 6_{2,5} - 6_{1,6}$	No	94.665	5.51e-16	1.2e-16	0.029	0.034	0.829
	94.705	702.3	$\nu = 0, 4_{4,1} - 4_{3,2}$	No	94.725	6.39e-16	1.4e-16	0.035	0.034	1.009
	95.176	1957.2	$\nu = 0, 9_{4,5} - 8_{5,4}$	No	95.193	2.78e-16	7.6e-17	0.029	0.034	0.854
	97.785	5003.7	$\nu = 2, 5_{1,5} - 4_{0,4}$	Yes^{p}	97.804	1.50e-16	4.2e-17	0.021	0.033	0.628
	98.232	2506.9	$\nu = 1, 2_{2,1} - 1_{1,0}$	No	98.254	2.87e-16	6.9e-17	0.036	0.033	1.103
	98.494	878.2	$\nu = 0, 5_{4,1} - 5_{3,2}$	No	98.511	3.05e-16	7.0e-17	0.029	0.033	0.880
R1A	104.094	933.8	$\nu = 0, 6_{3,4} - 6_{2,5}$	No	104.098	1.39e-16	5.8e-17	0.064	0.111	0.575
	107.704	2878.9	$\nu = 1, 5_{0,5} - 3_{3,0}$	No	107.745	1.74e-16	6.8e-17	0.094	0.113	0.838
	108.073	194.1	$\nu = 0, 2_{2,1} - 1_{1,0}$	No	108.100	1.69e-15	3.4e-16	0.112	0.113	0.992
	111.483	2621.0	$\nu = 1, 4_{1,4} - 3_{0,3}$	Yes^{p}	111.586	3.13e-16	8.6e-17	0.163	0.114	1.429
	112.511	1339.9	$\nu = 0, 7_{4,3} - 7_{3,4}$	No	112.550	1.53e-16	5.4e-17	0.099	0.115	0.859
	113.537	323.5	$\nu = 0, 4_{1,4} - 3_{0,3}$	No	113.538	1.51e-15	3.1e-16	0.119	0.115	1.036
	116.779	1212.0	$\nu = 0, 7_{3,4} - 6_{4,3}$	No	116.789	5.88e-16	1.4e-16	0.141	0.116	1.207
	121.722	550.4	$\nu = 0, 4_{3,2} - 4_{2,3}$	No	121.732	3.57e-16	8.3e-17	0.104	0.118	0.882
	127.884	1125.8	$\nu = 0, 7_{2,5} - 7_{1,6}$	No	127.907	1.24e-16	4.4e-17	0.091	0.120	0.757
	132.408	432.2	$\nu = 0, 4_{2,3} - 4_{1,4}$	No	132.453	5.17e-16	1.1e-16	0.116	0.122	0.950
	133.549	1447.6	$\nu = 0, 8_{3,6} - 7_{4,3}$	No^{m}	133.563	3.40e-16	8.1e-17	0.101	0.122	0.830
	134.935	574.8	$\nu = 0, 5_{1,4} - 5_{0,5}$	No	134.966	3.08e-16	7.4e-17	0.140	0.123	1.142
	136.496	410.7	$\nu = 0, 3_{3,0} - 3_{2,1}$	No	136.513	4.46e-16	1.0e-16	0.147	0.123	1.196
R1B	156.265	642.5	$\nu = 0, 5_{2,3} - 4_{3,2}$	Yes^{p}	156.262	1.25e-15	2.5e-16	0.156	0.126	1.240
	159.051	1615.4	$\nu = 0, 8_{4,5} - 7_{5,2}$	No^{m}	159.090	3.16e-16	7.0e-17	0.094	0.126	0.744

Table continues in the next page.

Table B.2. continued.

Band	λ [μm]	E_{up} [K]	Transition ν, $J_{Ka,Kc} - J_{Ka,Kc}$	Blend -	Central λ of fit [μm]	Flux [W m^{-2}]	Error [W m^{-2}]	FWHM [μm]	PACS FWHM [μm]	Ratio -
	160.510	732.1	$\nu = 0, 5_{3,2} - 5_{2,3}$	No	160.531	2.80e-16	6.4e-17	0.107	0.126	0.853
	166.815	1212.0	$\nu = 0, 7_{3,4} - 7_{2,5}$	Yes[o]	166.823	1.70e-16	4.3e-17	0.148	0.125	1.181
	166.827	5428.8	$\nu = 2, 6_{2,4} - 6_{1,5}$	Yes[o]	166.823	1.70e-16	4.3e-17	0.148	0.125	1.181
	170.928	2413.0	$\nu = 1, 2_{1,2} - 1_{0,1}$	No	170.957	1.27e-16	3.5e-17	0.140	0.125	1.123
	174.626	196.8	$\nu = 0, 3_{0,3} - 2_{1,2}$	No[m]	174.641	1.29e-15	2.6e-16	0.121	0.124	0.974
	179.527	114.4	$\nu = 0, 2_{1,2} - 1_{0,1}$	No	179.553	1.11e-15	2.2e-16	0.100	0.122	0.820
	180.488	194.1	$\nu = 0, 2_{2,1} - 2_{1,2}$	No	180.514	4.41e-16	9.2e-17	0.115	0.122	0.942

Table B.3. Extracted p-$H_2^{16}O$ lines from the PACS observations. The blended and masering lines are given as in Table B.2.

Band	λ [μm]	E_{up} [K]	Transition ν, $J_{Ka,Kc} - J_{Ka,Kc}$	Blend -	Central λ of fit [μm]	Flux [W m^{-2}]	Error [W m^{-2}]	FWHM [μm]	PACS FWHM [μm]	Ratio -
B2A	56.325	1048.5	$\nu = 0, 4_{3,1} - 3_{2,2}$	No	56.327	1.80e-15	3.8e-16	0.036	0.039	0.921
	59.987	1708.9	$\nu = 0, 7_{2,6} - 6_{1,5}$	Yes	59.994	1.75e-15	4.1e-16	0.060	0.039	1.539
	60.162	2273.8	$\nu = 0, 8_{2,6} - 7_{3,5}$	Yes	60.189	1.51e-15	4.5e-16	0.109	0.039	2.774
	60.989	2631.5	$\nu = 1, 3_{3,1} - 2_{2,0}$	No	60.985	7.21e-16	1.9e-16	0.037	0.039	0.934
	61.809	552.3	$\nu = 0, 4_{3,1} - 4_{0,4}$	No	61.801	1.05e-15	2.4e-16	0.035	0.039	0.886
	62.432	1554.5	$\nu = 0, 9_{2,8} - 9_{1,9}$	Yes[o]	62.447	1.28e-15	3.6e-16	0.094	0.039	2.392
	63.458	1070.6	$\nu = 0, 8_{0,8} - 7_{1,7}$	No	63.468	7.12e-16	2.0e-16	0.040	0.039	1.005
	63.928	1503.7	$\nu = 0, 6_{6,0} - 6_{5,1}$	Yes[o,p]	63.940	1.36e-15	4.6e-16	0.057	0.039	1.439
	63.949	3363.2	$\nu = 1, 8_{0,8} - 7_{1,7}$	Yes[o,p]	63.940	1.36e-15	4.6e-16	0.057	0.039	1.439
	67.089	410.4	$\nu = 0, 3_{3,1} - 2_{2,0}$	Yes	67.094	2.05e-15	4.2e-16	0.054	0.039	1.370
	71.067	598.9	$\nu = 0, 5_{2,4} - 4_{1,3}$	No	71.062	1.20e-15	2.5e-16	0.037	0.039	0.949
B2B	71.540	843.8	$\nu = 0, 7_{1,7} - 6_{0,6}$	No	71.561	9.60e-16	2.1e-16	0.033	0.039	0.839
	71.783	3138.2	$\nu = 1, 7_{1,7} - 6_{0,6}$	Yes[p]	71.807	5.17e-16	1.5e-16	0.040	0.039	1.028
	71.788	1067.7	$\nu = 0, 5_{5,1} - 6_{2,4}$	Yes[p]	71.807	5.17e-16	1.5e-16	0.040	0.039	1.028
	78.928	781.2	$\nu = 0, 6_{1,5} - 5_{2,4}$	No	78.951	1.45e-15	3.1e-16	0.042	0.039	1.096
	80.222	1929.3	$\nu = 0, 9_{4,6} - 9_{3,7}$	No	80.238	3.36e-16	1.1e-16	0.042	0.038	1.096
	80.557	1807.1	$\nu = 0, 8_{5,3} - 8_{4,4}$	No	80.587	2.43e-16	1.0e-16	0.050	0.038	1.314
	81.216	1021.0	$\nu = 0, 7_{2,6} - 7_{1,7}$	No	81.223	5.97e-16	1.4e-16	0.044	0.038	1.148
	81.690	1511.0	$\nu = 0, 8_{3,5} - 7_{4,4}$	Yes	81.726	5.78e-16	1.7e-16	0.051	0.038	1.329
	81.893	3088.1	$\nu = 1, 6_{1,5} - 5_{2,4}$	Yes	81.919	5.51e-16	1.7e-16	0.055	0.038	1.428
	83.284	642.7	$\nu = 0, 6_{0,6} - 5_{1,5}$	No	83.295	1.66e-15	3.4e-16	0.036	0.038	0.949
	84.068	2937.8	$\nu = 1, 6_{0,6} - 5_{1,5}$	No	84.086	4.68e-16	1.1e-16	0.044	0.038	1.154
	85.781	3452.0	$\nu = 1, 6_{4,2} - 6_{3,3}$	Yes[o]	85.796	4.10e-16	9.4e-17	0.033	0.037	0.872
	89.988	296.8	$\nu = 0, 3_{2,2} - 2_{1,1}$	No	89.998	2.08e-15	4.4e-16	0.040	0.036	1.109
	92.150	2508.6	$\nu = 1, 2_{2,0} - 1_{1,1}$	No	92.175	4.84e-16	1.0e-16	0.035	0.035	0.998
	93.383	1175.1	$\nu = 0, 7_{3,5} - 7_{2,6}$	Yes	93.380	7.13e-16	1.5e-16	0.059	0.035	1.681
	94.210	877.9	$\nu = 0, 5_{4,2} - 5_{3,3}$	Yes[o]	94.222	5.34e-16	1.2e-16	0.055	0.035	1.587
	94.897	2766.7	$\nu = 1, 5_{1,5} - 4_{0,4}$	Yes	94.899	6.06e-16	1.3e-16	0.071	0.034	2.057
	95.627	470.0	$\nu = 0, 5_{1,5} - 4_{0,4}$	Yes	95.643	1.97e-15	4.0e-16	0.050	0.034	1.454
R1A	111.628	598.9	$\nu = 0, 5_{2,4} - 5_{1,5}$	No	111.617	2.29e-16	8.2e-17	0.097	0.114	0.853
	113.948	725.1	$\nu = 0, 5_{3,3} - 5_{2,4}$	No	113.962	3.16e-16	8.1e-17	0.120	0.115	1.037
	125.354	319.5	$\nu = 0, 4_{0,4} - 3_{1,3}$	No	125.383	1.03e-15	2.1e-16	0.126	0.120	1.054
	126.714	410.4	$\nu = 0, 3_{3,1} - 3_{2,2}$	Yes	126.689	3.22e-16	8.5e-17	0.206	0.120	1.717
	128.259	2615.0	$\nu = 1, 4_{0,4} - 3_{1,3}$	Yes	128.284	2.59e-16	7.3e-17	0.192	0.121	1.594
	138.528	204.7	$\nu = 0, 3_{1,3} - 2_{0,2}$	No[m]	138.549	1.02e-15	2.1e-16	0.125	0.123	1.010
R1B	144.518	396.4	$\nu = 0, 4_{1,3} - 3_{2,2}$	No	144.555	7.65e-16	1.6e-16	0.109	0.125	0.876
	146.923	552.3	$\nu = 0, 4_{3,1} - 4_{2,2}$	No	146.946	2.16e-16	4.8e-17	0.106	0.125	0.851
	156.194	296.8	$\nu = 0, 3_{2,2} - 3_{1,3}$	Yes[o]	156.262	1.25e-15	2.5e-16	0.152	0.126	1.210
	167.035	867.3	$\nu = 0, 6_{2,4} - 6_{1,5}$	No	167.063	7.87e-17	2.5e-17	0.091	0.125	0.727
	169.739	1175.1	$\nu = 0, 7_{3,5} - 6_{4,2}$	No	169.764	2.14e-16	4.7e-17	0.101	0.125	0.806
	170.139	951.9	$\nu = 0, 6_{3,3} - 6_{2,4}$	No	170.160	1.67e-16	4.5e-17	0.125	0.125	1.001
	187.111	396.4	$\nu = 0, 4_{1,3} - 4_{0,4}$	No	187.124	1.58e-16	3.4e-17	0.086	0.119	0.721